www.small-structures.com

Blended Salt Electrolyte Design for Enhanced NMC811||Graphite Cell Performance

Peng Yan, Mykhailo Shevchuk, Christian Wölke, Felix Pfeiffer, Debbie Berghus, Masoud Baghernejad, Gerd-Volker Röschenthaler, Martin Winter, and Isidora Cekic-Laskovic*

The high energy density, nickel-rich layered cathode material LiNio 8Mno 1Coo 1O2 (NMC811) is recognized as a promising candidate for next-generation battery chemistries. However, due to their structural and interfacial instability, nickel-rich NMC cathodes still face a number of challenges in practical application. For this reason, the design and development of novel electrolyte formulations, able to stabilize the nickel-rich cathodelelectrolyte interface, are highly demanded. In this work, a novel electrolyte is developed using lithium (difluoromethanesulfonyl) (trifluoromethanesulfonyl)imide (LiDFTFSI) and lithium hexafluorophosphate (LiPF₆) as salt blend in an organic carbonate-solvent based solvent mixture. The presence of LiDFTFSI notably enhances the electrochemical performance of the resulting NMC811||graphite cells. Further advancement of the considered cell chemistry is achieved by introducing the well-known functional electrolyte additive vinylene carbonate (VC), which was found to feature a synergistic effect with LiDFTFSI. The formation of a homogenous, effective, and robust solid electrolyte interphase (SEI) as well as cathode electrolyte interphase (CEI) on the corresponding electrodes resulted in superior electrochemical performance.

1. Introduction

Lithium-ion batteries (LIBs) are becoming increasingly important as energy storage systems, and the growing demands of

P. Yan, C. Wölke, F. Pfeiffer, M. Baghernejad, M. Winter, I. Cekic-Laskovic Forschungszentrum Jülich GmbH
Helmholtz-Institute Münster (IEK-12)
Corrensstraße 48, 48149 Münster, Germany
E-mail: i.cekic-laskovic@fz-juelich.de

M. Shevchuk, G.-V. Röschenthaler School of Science Constructor University Bremen GmbH Campus Ring 1, 28759 Bremen, Germany

D. Berghus, M. Winter MEET Battery Research Center University of Münster Corrensstraße 46, 48149 Münster, Germany

The ORCID identification number(s) for the author(s) of this article can be found under https://doi.org/10.1002/sstr.202300425.

© 2023 The Authors. Small Structures published by Wiley-VCH GmbH. This is an open access article under the terms of the Creative Commons Attribution License, which permits use, distribution and reproduction in any medium, provided the original work is properly cited.

DOI: 10.1002/sstr.202300425

the grid storage, automotive, and portable consumer markets require batteries with ever higher energy densities. To achieve this, one promising approach addresses the employment of high-capacity layered transition metal oxide cathodes, such as nickel-rich LiNi_{0.8}Mn_{0.1}Co_{0.1}O₂ (NMC811) which can deliver a high reversible specific capacity of $>180 \,\mathrm{mAh}\,\mathrm{g}^{-1}$. However, due to its structural and interfacial instabilities, these nickel-rich NMC cathode materials still face challenges in long-term galvanostatic cycling.[3] In addition, the state-of-the-art (SOTA) electrolyte for LIBs containing lithium hexafluorophosphate (LiPF₆) salt dissolved in a mixture of cyclic and linear carbonates represents another major challenge with respect to long-term galvanostatic cycling performance. [4,5] Among others, the decomposition of thermally unstable LiPF₆ leads to the formation of pentafluorophosphorane (PF₅). LiPF₆ and PF₅ react with residual H₂O

and form HF which can trigger detrimental processes such as organofluorophosphate formation $^{[6]}$ and transition metal dissolution, thus deteriorating overall battery performance and safety. $^{[7,8]}$ More importantly, the ineffective interphase derived by the LiPF₆-based electrolyte is prone to cracking, which in turn leads to the consumption of active lithium to reform the surface interphase during prolonged galvanostatic cycling. $^{[9,10]}$

For these reasons, the design of novel electrolyte formulations, which enable the formation of an effective cathode electrolyte interphase (CEI),[11] is highly desirable. It is worth noting that in previous studies, CEI formation has typically been treated as a standalone process, that is independent of the solid electrolyte interphase (SEI) formation on the anode. Recent research studies point to the cross-talk between the cathode and anode. [7,8,12,13] The observation of transition metal dissolution from the cathode, which affects the interphase on both electrodes, further supports the existence of the cross-talk.^[7,8] Similar to the cross-talk from the cathode to the anode side, the evolution of the SEI on the anode side can also impact the formation of the CEI on cathode side. Studies by Zhang et al. have demonstrated the dynamic evolution of CEI upon charge/discharge and have shown a positive correlation between CEI and SEI. [12] In addition, Fang et al. have proposed a CEI formation pathway via the



www.small-structures.com

migration of surface species originally formed on the anode side. [13] Although a comprehensive understanding of cross-talk between electrodes remains a challenge, it is clear that the establishment of an effective SEI/CEI pair is essential to achieving a long and stable cycle life in batteries with nickel-rich NMC cathode materials. Electrolyte optimization plays a crucial role in facilitating the formation of a desirable SEI/CEI pair, leading to improved battery performance and longevity.

The most common and economically feasible way of optimizing electrolytes is to introduce functional additives into the baseline formulation. For example, vinylene carbonate (VC) is often used as a film-forming additive to stabilize the SEI on a graphitebased electrode, whereas lithium difluorophosphate (LiDFP) can facilitate a protective CEI layer on a Ni-rich cathode. [10,14-16] The challenges arising from the commonly used conducting salt. LiPF₆, remain partially unsolved. Numerous studies have been conducted to substitute LiPF6 with alternatives such as sulfonimide salts lithium bis(fluorosulfonyl)imide (LiFSI) and lithium bis(trifluoromethanesulfonyl)imide (LiTFSI), which are thermally stable and insensitive to moisture. [4,17,18] In addition, these two conducting salts allow for an ionic conductivity of the resulting electrolyte formulations comparable to SOTA electrolyte formulations. [4,19,20] The shortcoming of electrolytes containing LiFSI or LiTFSI however is related to the dissolution of the Al current collector at potentials >3.8 V versus Li|Li+ for LiTFSI and >4.0 V versus Li|Li $^+$ for LiFSI. $^{[4,19,21]}$

Armand et al. recently introduced lithium (difluoromethane-sulfonyl) (trifluoromethanesulfonyl)imide (LiDFTFSI), in which one fluorine atom is replaced by hydrogen compared to LiTFSI. LiDFTFSI was found to exhibit an excellent passivation ability toward the Al current collector at potentials of >4.2 V versus Li|Li⁺.^[22] In addition, the electrochemically labile CF₂H moiety in LiDFTFSI undergoes decomposition, leading to the formation of advantageous SEI on the Li metal electrode. This SEI formation results in the improved electrochemical performance of Li metal batteries. ^[22–26] However, there is currently a lack of systematic research investigating the potential impact of LiDFTFSI on the cathode as well as the resulting CEI formation and dynamics.

Here, a blended salt strategy was adopted by incorporating LiDFTFSI into a LiPF₆-based electrolyte, thus leading to a substantial advancement in the performance of the resulting NMC811||graphite cells. Additionally, further performance enhancement can be achieved by the addition of VC to the blended salt electrolyte. Comprehensive electrochemical and post-mortem analysis revealed that the LiDFTFSI alone can effectively mitigate the structural changes in the NMC811 electrode during prolonged galvanostatic cycling by facilitating the formation of a modified CEI. However, the continued growth of inhomogeneous CEI remains challenging. Interestingly, the addition of VC induces a synergistic effect with LiDFTFSI that leads to the formation of an effective, homogenous, and robust CEI. As a result, NMC811||graphite cells using electrolyte containing LiDFTFSI and VC can achieve 720 cycles at 1C while maintaining 80% state-of-health (SOH_{80%}), whereas cells with SOTA electrolytes only achieve 200 cycles.

2. Results and Discussions

2.1. Impact of LiDFTFSI on the NMC811||Graphite Cell Chemistry

To investigate the impact of LiDFTFSI on NMC811||graphite cell chemistry, the long-term galvanostatic cycling stability of corresponding cells was evaluated as depicted in Figure 1a. Cells with baseline electrolyte (BE) exhibit an initial specific discharge capacity of approximately 200 mAh g⁻¹ in the first cycle. However, a rapid decline becomes evident after 50 cycles, and the SOH_{80%} is reached after 200 cycles (Figure S3, Supporting Information). Further galvanostatic cycling results in a 27.4% capacity retention after 500 cycles at a specific discharge capacity of 51.1 mAh g^{-1} . The cells containing BE + DFTFSI initially deliver a slightly lower specific discharge capacity of approximately 195 mAh g⁻¹ compared to cells with BE, but, show an improved galvanostatic cycling performance with a 77.9% capacity retention and a specific discharge capacity of 142 mAh g⁻¹ after 500 cycles. The positive effect of LiDFTFSI results in a notably improved galvanostatic cycling performance compared to the BE counterpart. It can be noticed that cells containing the BE + DFTFSI electrolyte have a slightly decreased Coulombic efficiency (C_{Fff}) in the first cycle compared to considered counterparts due to the higher consumption of active lithium for possible SEI and CEI formation. [22,23] The improved C_{Eff} of cells with BE+DFTFSI during continued galvanostatic cycling also suggests a beneficial impact of LiDFTFSI on the electrode|electrolyte inteface. The same trend can also be observed from the charge-discharge profile of selected cycles where BE has a notably increased overvoltage after 100 cycles with faster capacity fading as seen in Figure 1b. The shift of charge and discharge capacity endpoints results from cascade side reactions can be used to study possible degradations phenomena during galvanostatic cycling. [27] In the capacity marching plot (Figure 1c,e), the charge and discharge endpoints are calculated by using the cumulative capacity as a function of cycle number as calculated by the following equations^[27,28]:

Cumulated
$$Q_{CN} = Q_{C0} + \Delta Q_{C1} + \Delta Q_{C2} + \dots + \Delta Q_{C(N-1)} (\text{at cycle } N)$$
 (1)

Cumulated
$$Q_{\rm DN}=Q_{\rm D0}+\Delta Q_{\rm D1}+\Delta Q_{\rm D2}+\ldots +\Delta Q_{\rm D(N-1)}({\rm at\,cycle}\,N)$$
 (2)

with
$$\Delta Q_{CN} = Q_{CN} - Q_{C(N-1)}$$
 and $\Delta Q_{DN} = Q_{DN} - Q_{D(N-1)}$

The calculated charge and discharge endpoints for corresponding cycles are marked in Figure 1b,c. As shown in Figure 1c, the discharge capacity endpoint (Q_D) increases with a large slope which indicates side reactions at the negative electrode, $^{[27,29]}$ and in turn suggests continuous SEI formation due to the ineffective SEI formed by the BE. Furthermore, the charge capacity endpoint (Q_C) of cells containing BE initially marches rapidly to higher values but decreases to a lower capacity endpoint during continued galvanostatic cycling. The marching of Q_C indicates an oxidation side reaction on the positive electrode which allows the cumulative capacity to grow larger than the

26884062, 2024, 4, Downloaded

from https://onlinelibrary.wiley.com/doi/10.1002/sstr.202300425 by Forse

Jülich GmbH Research Center, Wiley Online Library on [07/05/2024]. See the Terms

on Wiley Online Library for rules of use; OA articles are governed by the applicable Creative Commons I

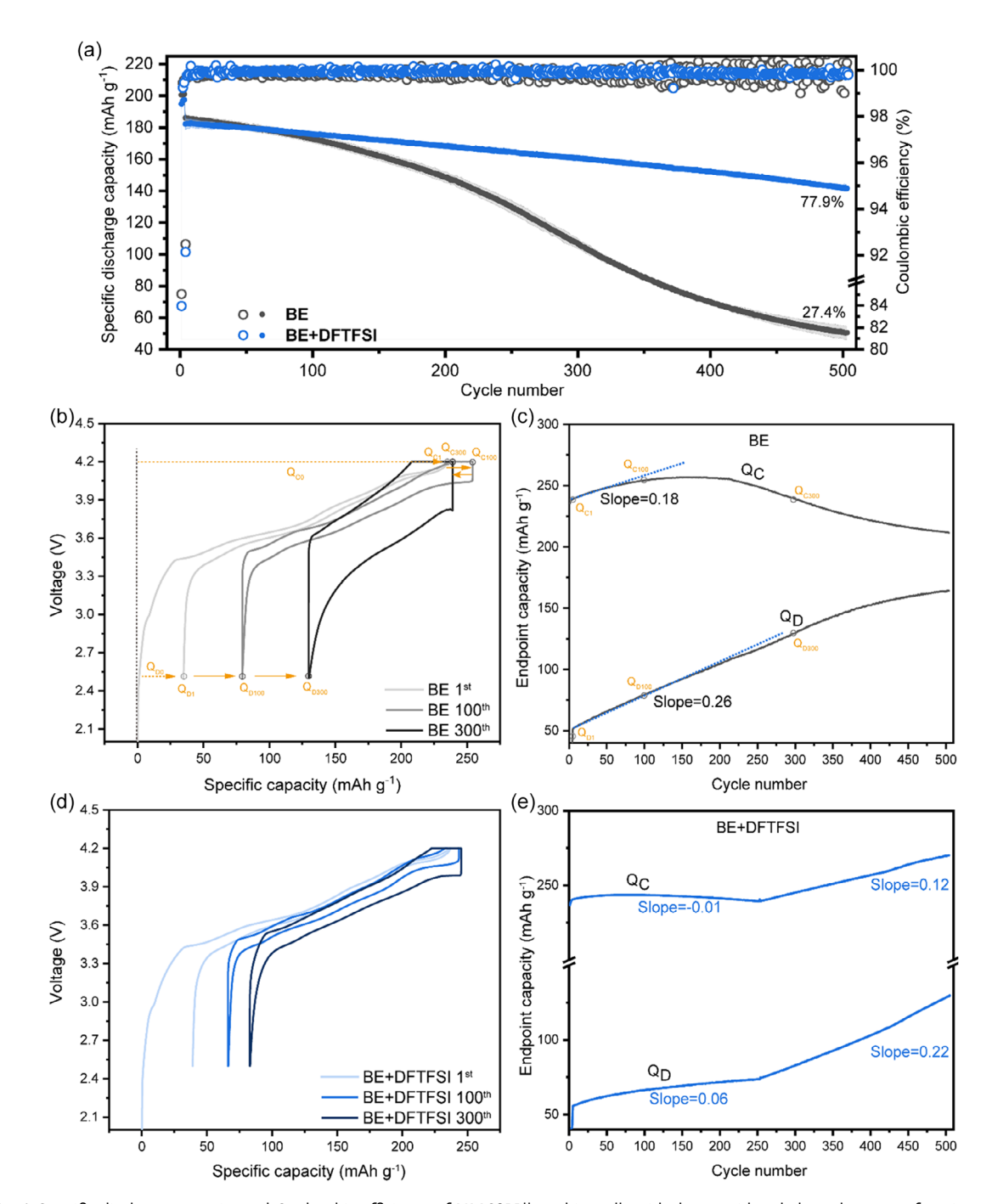


Figure 1. a) Specific discharge capacity and Coulombic efficiency of NMC811||graphite cells with the considered electrolytes as a function of the cycle number; 80% SOC is considered as the end of life. Electrochemical charge-discharge profile of NMC811||graphite cells in b) BE and d) BE + DFTFSI. The charge and discharge endpoints of the considered cells with c) BE and e) BE + DFTFSI are plotted using cumulative capacity versus cycle number.

theoretical one, whereas a decrease in the marching of $Q_{\rm C}$ might be explained by several reasons: a decrease in the rate of side reactions at the cathode; an increase in cell impedance; and an increase in the rate of the loss of cathode active materials. [27,28] In the case of cells containing BE, the decrease of $Q_{\rm C}$ and rapid increase of $Q_{\rm D}$ result in a narrow capacity window ($Q_{\rm C}$ – $Q_{\rm D}$) which results in a lower discharge capacity.

To further confirm the degradation mechanism, derivative voltage analysis (DVA) and incremental capacity analysis (ICA) were conducted. The $\mathrm{d}V/\mathrm{d}Q$ curve in the DVA analysis was used to provide an estimation of the loss of lithium inventory (LLI) and the loss of active materials (LAM) whereas the $\mathrm{d}Q/\mathrm{d}V$ plots within the ICA analysis were used to study the irreversible transition of active materials and the rise of impedance. [30–35]

www.small-structures.com

Figure 3a shows the ICA of a cell containing BE. The intensity of peaks decreases quickly during continuous galvanostatic cycling and the dominant phase transitions of $M \rightarrow H_2$ and $H_2 \rightarrow H_3$ cannot be observed after 200 cycles, thus revealing the LAM from both the anode and the cathode. In addition, the large peak shift indicates the rise of impedance which can originate from both the LAM or the LLI. [27] Figure 3c shows the DVA of a cell with BE, where the shift of peaks with the increase of cycle numbers becomes apparent. To distinguish between the contributions from the anode and the cathode for different peaks, a threeelectrode cell was assembled and cycled at 0.1 C to identify the corresponding positions as observed in the DVA plot of a three-electrode system in Figure 2. The DVA of the anode exhibits two narrow peaks, marked as AN1 and AN2 whereas the DVA of the cathode shows two broad peaks marked as CA1 and CA2. As can be seen, there are distances between the peaks that are directly proportional to the active material capacity. [36] The distance D2 can be used to estimate the loss of cathode active material whereas information on the remaining capacity of the anode active material can be obtained from the distance D3.[37] However, due to the difficulty of locating peak AN1 in the full cell, the left shift of the anode peak AN2 - which is the reduction of distance D1 - can be used to describe the LLI. As shown in **Figure 3c**, the cell containing BE shows large $\Delta D2$ and $\Delta D1$ values starting from the 200th cycle, which indicates LAM from the cathode and LLI caused by an ineffective SEI. Furthermore, the absence of the peak denoted by the red and blue arrows further confirms the LAM. Together with the large LLI, this leads to the rise of impedance indicated by the shift of the phase transition peaks as seen in the dQ/dV plot in Figure 3a, thus resulting in a pronounced increase of cell polarization (ΔV) in Figure S1, Supporting Information.

In the case of BE + DFTFSI, a substantially lower overvoltage and capacity fading can be observed in the charge-discharge profile (Figure 1d). In addition, a slower increase of Q_D (as shown in Figure 1e) indicates fewer side reactions at the anode and thus suggests the formation of an effective SEI on the graphite

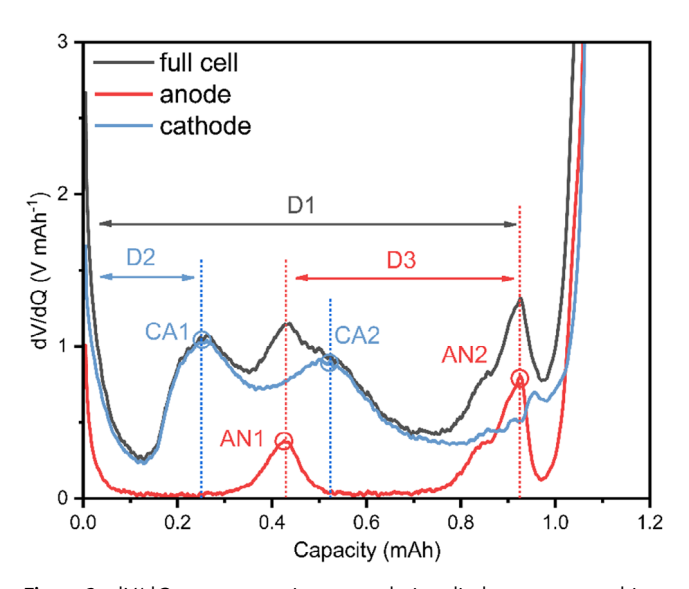


Figure 2. dV/dQ versus capacity curves during discharge measured in a three-electrode setup.

electrode by decomposition products from LiDFTFSI. Interestingly, an almost constant Q_C is observed, which can be attributed to suppressed side reactions on the cathode electrode, possibly due to the formation of an effective CEI. However, a knee point appears after \approx 250 cycles and both Q_C and QD start marching, which means that pronounced side reactions were triggered on both electrodes. Considering the previously stable Q_{C} , the appearance of a knee point could potentially be explained by the breakdown of the CEI, which might influence the anode via the interfacial cross-talk. [38,39] Nevertheless, only slightly faster capacity fading after 250 cycles is apparent in Figure 1a. This observation does not imply that the appearance of the knee point has no impact on the galvanostatic cycling performance, but rather indicates that the cells enter a "metastable state" after the onset of the knee point and any further degradation might trigger a pronounced fading. [27] From the ICA of a cell with BE + DFTFSI, a decrease of the phase transition peaks from cathode ($H_1 \rightarrow M$, $H_2 \rightarrow H_3$) becomes evident during prolonged galvanostatic cycling, but it is delayed compared to BE and could still be observed on the 300th cycle (Figure 3b). In addition, the larger $\Delta D2$ observed after the 200th cycle in the DVA plot depicted in Figure 3d further supports the assumption that the knee point appears at 250 cycles as a structural change of the NMC811 electrode, specifically associated with the breakdown of the formed CEI. Furthermore, the continued increase of $\Delta D1$ suggests a continuous LLI. Finally, a relatively low cell polarization (ΔV) was observed for the initial galvanostatic cycling, which increased after 100 cycles and may indicate beginning of the CEI breakdown (Figure S1, Supporting Information). In conclusion, by introducing LiDFTFSI to the LiPF₆-based electrolyte formulation as a co-salt, the galvanostatic cycling performance of NMC811||graphite cell chemistry can be notably enhanced, due to the beneficial effect of LiDFTFSI on both the SEI and the CEI. However, the fading rate starts increasing at ≈250 cycles, thus indicating the insufficient long-term stability of the formed CEI.

To investigate the effect of LiDFTFSI on the cell/electrode performance and to further understand the possible reason for the appearance of the knee point, the resistance and morphology of the graphitelelectrolyte as well as the NMC811|electrolyte interface after the formation cycles and after 100 cycles were characterized by electrochemical impedance spectroscopy (EIS) and scanning electron microscopy (SEM). Considering the contribution of both the anode and the cathode in the EIS measurements, it is difficult to make a clear distinction in a full cell setup. An EIS approach with symmetric coin cells as described by Petibon et al. [40] was therefore utilized. Figure 4a,d show the Nyquist plots of graphite||graphite and NMC811||NMC811 cells after formation cycles and after 100 cycles. Two clearly distinguishable semicircles can be observed for the NMC811||NMC811 cells, whereas the graphite||graphite cells show less pronounced features. The first semicircle in the high-frequency range is typically assigned in literature to the resistance of interphases. [10,37] However, recent studies have indicated that the resistance of electrodeto-current collector interface also contributes to the highfrequency semicircle. [41-43] Despite this, the contact resistance is usually lower than the interphase resistance, and for the purposes of this study, the first semicircle is considered only as the resistance of the interphase. [44,45] The semicircle observed at

from https://onlinelibrary.wiley.com/doi/10.1002/sstr.202300425 by Forse

Jülich GmbH Research Center, Wiley Online Library on [07/05/2024]. See the Terms and Conditions (https://onlinelibrary.wiley.com/term

conditions) on Wiley Online Library for rules of use; OA articles are governed by the applicable Creative Commons l

www.small-structures.com

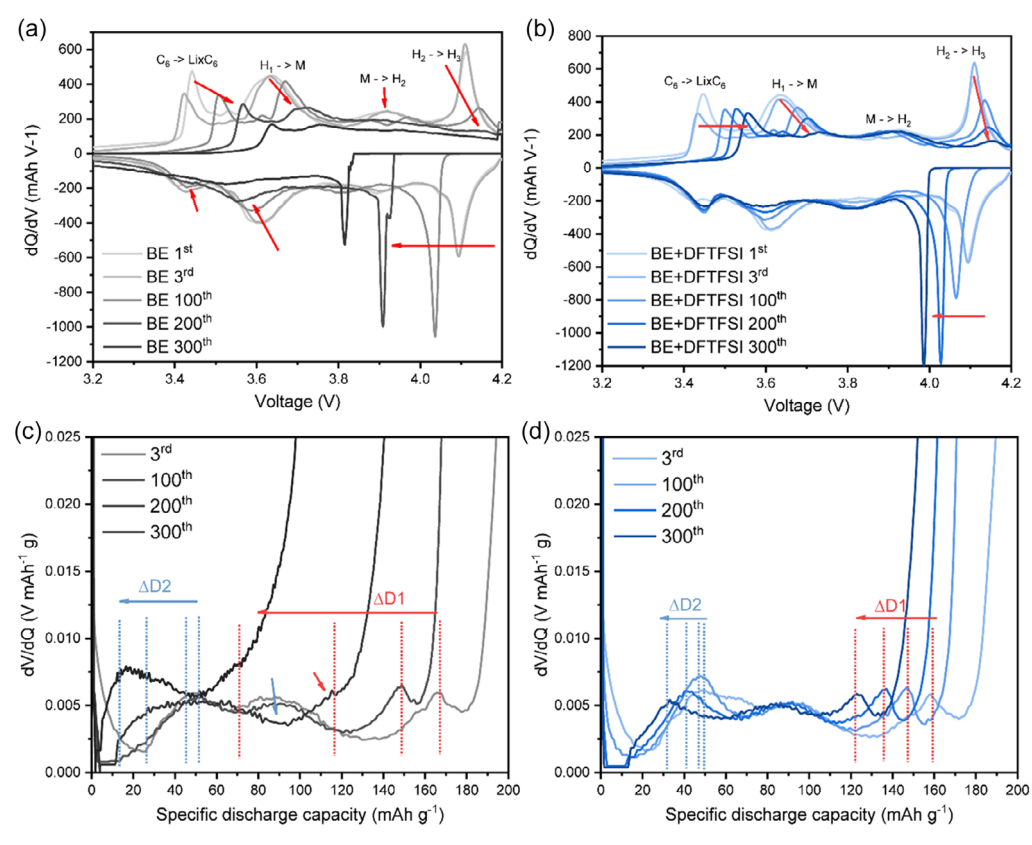


Figure 3. Differential capacity versus cell voltage plots of NMC811||graphite cells with a) BE and b) BE+DFTFSI at selected cycles. The peaks are assigned to their corresponding phase transitions. [65] M represents the monoclinic phase and H_1 , H_2 , and H_3 represent the hexagonal phases. $C_6 \rightarrow LiC_x$ arises from the lithiation of graphite. Differential voltage versus discharge capacity plots of NMC811||graphite cells with c) BE and d) BE+DFTFSI at different cycles.

middle frequency range is normally ascribed to charge transfer processes. With the equivalent circuit model (ECM) depicted in Figure S2, Supporting Information, the resistance of interphase $(R_{\text{SEI/CEI}})$ and resistance of charge transfer (R_{CT}) can be identified. It is evident that cells with BE exhibit a remarkable resistance increase on the NMC811 electrode after 100 cycles, with most of the increase stemming from the $R_{\rm CT}$ (Figure 4e). The increase in charge transfer resistance indicates a larger barrier for lithium migration and can be explained by the structural/surface changes of the active material. [37] In line with this, the increase of R_{CT} observed for BE can be explained by the LAM on the NMC811 electrode as discussed by ICA and DVA. In the case of electrodes harvested from cells with BE + DFTFSI, a lower increase in impedance for the NMC811 electrode can be observed compared to BE as illustrated in Figure 4d. However, it is important to note that a larger R_{CEI} is observed after the formation cycles which implies the contribution of LiDFTFSI in the CEI formation. Interestingly, R_{CEI} increases meaningfully after 100 cycles, indicating the growth of a resistive CEI. The formation of inhomogeneous depositions can be observed by SEM after the formation, which covers most of the NMC811 particles after 100 cycles (Figure S4g,h, Supporting Information). This goes hand in hand with the lower R_{CT} measured on harvested NMC811 electrodes from cells containing BE + DFTFSI, which further supports the DVA and ICA

results suggesting that LiDFTFSI may form a protective CEI, thus resulting in good structural stability and leading to less LAM on the NMC811 electrode. Nevertheless, the progressive growth of CEI raises the barrier for lithium charge transfer and results in pronounced electrolyte consumption. This leads to the occurrence of a knee point after $\approx\!250$ cycles, indicating that the formed CEI is ineffective to further protect the NMC811 electrode.

X-ray photoelectron spectroscopy (XPS) scans were conducted to identify the chemical composition of the corresponding interphases on graphite (SEI) and NMC811 (CEI) electrodes after formation cycles in cells containing BE and BE + DFTFSI. As shown in Figure 5, the signals of C 1s spectra of harvested graphite electrodes show peaks commonly attributed to the decomposition of solvents, which are C-C, C-O, C=O, O-C=O, and -CO₃- groups, with the corresponding peaks for the oxygen atoms in these groups detected in the O 1s spectra. Furthermore, additional peaks assigned to CF₃ and CF_x could be observed on the electrodes from cells with LiDFTFSI containing electrolyte, pointing at the participation of LiDFTFSI in the SEI formation. This is further confirmed by the presence of peaks in the N 1s and S 1s core spectra, whereas only noise is observed for the BE counterpart. Similar peaks related to the decomposition of solvents were also observed on NMC811 electrodes, as shown in Figure 5b. In addition, the peaks assigned to the decomposition

26884062, 2024, 4, Downloaded from https://onlinelibrary.wiley.com/doi/10.1002/sstr.202300425 by Forsch

um Jülich GmbH Research Center, Wiley Online Library on [07/05/2024]. See the Terms

and-conditions) on Wiley Online Library for rules of use; OA articles are governed by the applicable Creative Commons

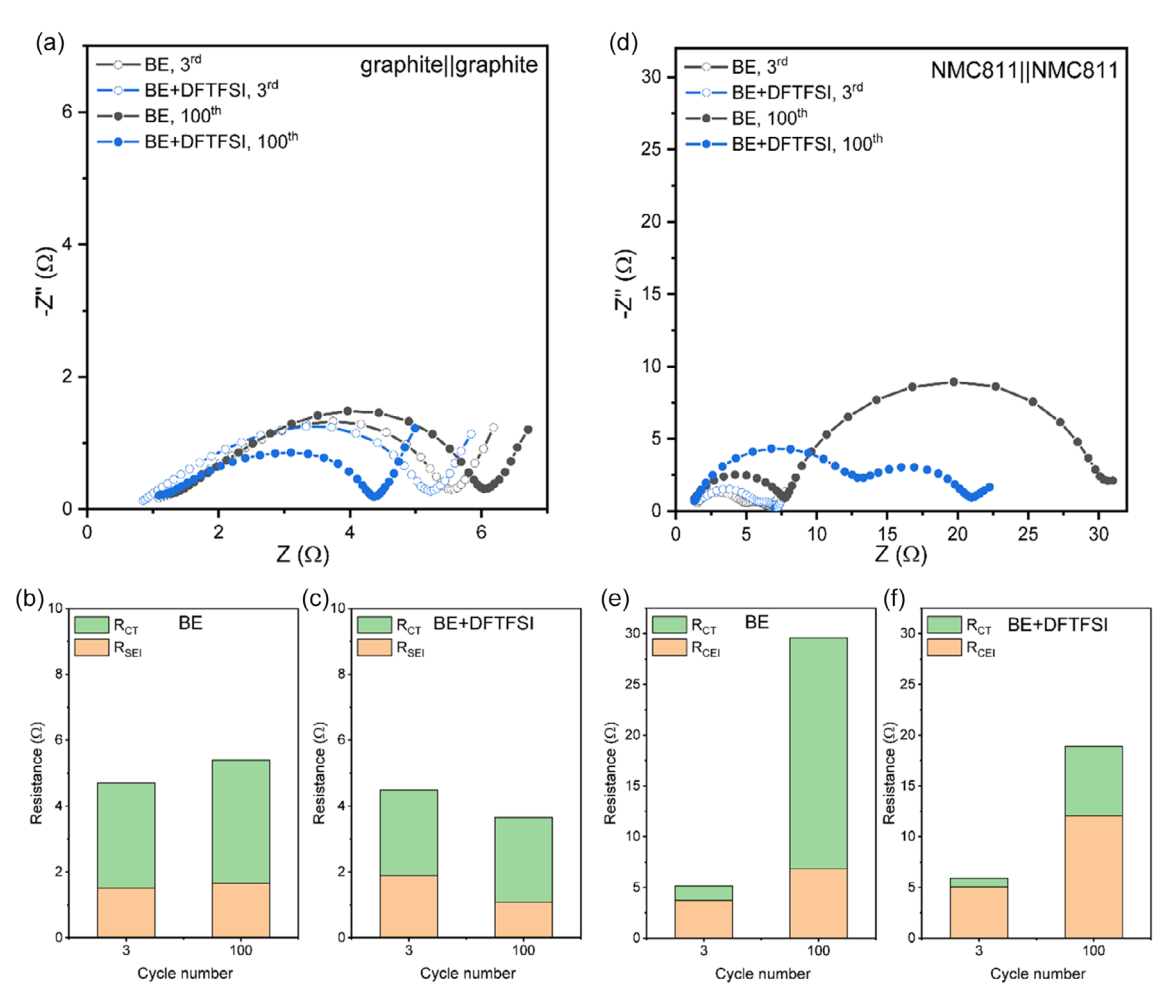


Figure 4. a) Nyquist plots for reassembled symmetric graphite cells after three formation cycles and after 100 cycles as well as fitted resistance for b) BE and c) BE + DFTFSI. d) Nyquist plot for reassembled symmetric NMC811 cells after three formation cycles and after 100 cycles and fitted resistance for e) BE and f) BE + DFTFSI.

products of LiDFTFSI were observed from the C 1s, N 1s, and S 2p core spectra in the case of BE + DFTFSI, suggesting the contribution of LiDFTFSI in the CEI formation. Theoretically, LiDFTFSI should undergo reduction and remain stable against oxidation. [22–24] The decomposition products from LiDFTFSI observed on the CEI can thus be attributed to the migration of SEI fragments from the anode to the cathode during the galvanostatic cycling process. [12,13,46–48] Notably, the signal assigned to LiF at 684 eV in the F 1s core spectra is prominent for the BE compared to the BE + DFTFSI counterpart in both the SEI and the CEI. This disparity could be attributed to the altered SEI and CEI compositions originating from the presence of LiDFTFSI.

To understand the changes in surface composition during the continued galvanostatic cycling, additional XPS measurements were conducted for graphite and NMC811 electrodes after 100 cycles. Observations made for XPS spectra of electrodes from cells galvanostatically cycled with BE, along with the insights gained from ICA and DVA, point to the ineffective SEI formation that undergoes cracking and reforming during the galvanostatic cycling for cells containing BE. As a result, the electrolyte is continuously consumed and cross-talk can be observed between the

anode and the cathode. The detailed results of the surface composition of cells containing BE, as observed by XPS spectra, are provided in the SI. Figure 6 shows the XPS spectra of graphite and NMC811 electrodes with the BE + DFTFSI after formation cycles (blue) and after 100 cycles (black). The peaks related to the decomposition products of the considered solvents, as observed in C 1s and O 1s core spectra of the graphite electrode, only show minor changes during galvanostatic cycling. Similarly, the peak assigned to Li_xPF_v from the P 2p core spectra of the graphite electrode also exhibits minor changes during galvanostatic cycling. These observations suggest a reduced decomposition of the considered solvents and LiPF₆ compared to BE. This is also supported by the similar trend for peaks assigned to the solvent and LiPF₆ observed in the NMC811 electrode. However, on the graphite electrode surface, the peaks assigned to the LiDFTFSI or its decomposition products, such as CF3 from C 1s spectra, [DFTFSI] from N 1s spectra, and SO_x from S 2p spectra, show a decrease in intensity after prolonged galvanostatic cycling. Interestingly, on the NMC811 electrode the same peaks exhibit an increasing intensity. This observation could either indicate that LiDFTFSI does not contribute to later stages of SEI

elibrary.wiley.com/doi/10.1002/sstr.202300425 by Fors

Research Center, Wiley Online Library on [07/05/2024]. See the

on Wiley Online Library for rules of use; OA articles are governed by the applicable Creative Commons

www.advancedsciencenews.com www.small-structures.com



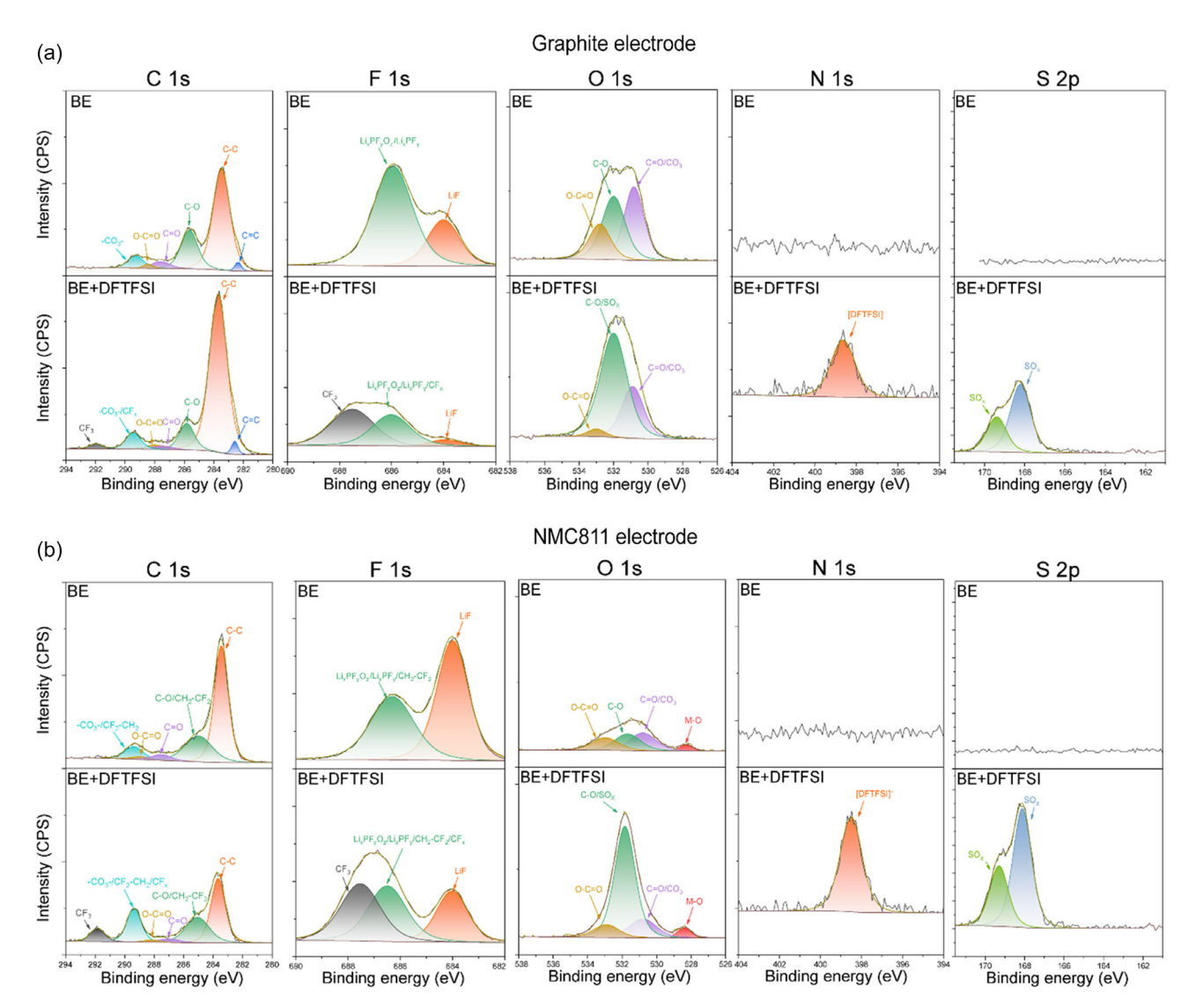


Figure 5. Selected XPS spectra of the harvested a) graphite and b) NMC811 electrodes from cells galvanostatically cycled with BE and BE + DFTFSI after formation cycles.

evolution, i. e. the originally formed SEI is gradually covered by species stemming from the solvent and LiPF $_6$, or that SEI species derived from LiDFTFSI migrate to the CEI over time. The CEI thickness can be calculated according to the method of Niehoff et al., as depicted in Figure S14, Supporting Information. Notably, for BE + DFTFSI, a remarkably thin CEI is observed after the formation cycles, thus underlining the effect of LiDFTFSI on the NMC811 electrode. However, after 100 cycles, the CEI thickness exhibits a substantial increase. This further supports the conclusion that the CEI formed is ineffective over longer periods of time, which ultimately leads to the observed knee point and change in galvanostatic cycling behavior.

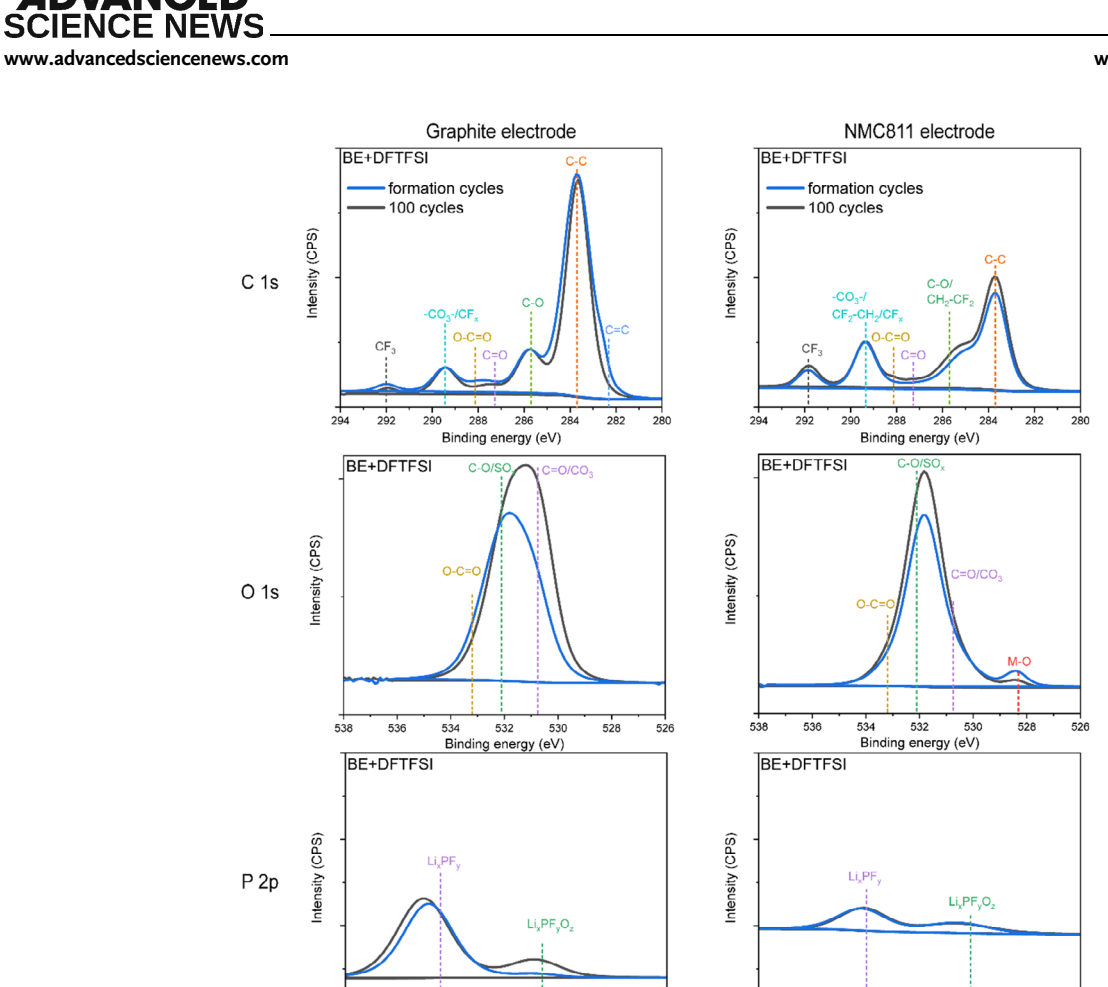
To determine the composition and the thickness of the SEI formed in the presence of the LiDFTFSI containing electrolyte, graphite electrodes were sputtered for a total duration of 720 s (2 times at 360 s, each). The peak assigned to C=C (\approx 282.0 eV) from the C 1s spectra corresponds to lithiated graphite. [50] Due to

the surface sensitivity of the XPS technique, the intensity of the lithiated graphite peak is higher when the graphite active material is closer to the electrode surface, i. e. when the SEI is thinner. The atomic concentration of the lithiated graphite can thus serve as an indicator of the thickness of the SEI (Figure S15, Supporting Information). For all electrodes, the atomic concentration of the C=C species is substantially lower compared to the pristine electrode, confirming the formation of an SEI after galvanostatic cycling as expected. By comparing graphite electrodes from cells galvanostatically cycled with BE and BE + DFTFSI after the formation cycles, a minimal atomic concentration of signal C=C is observed before etching for both electrodes. However, after etching, the atomic concentration is higher for the graphite electrode containing BE + DFTFSI, indicating that the presence of LiDFTFSI leads to the formation of a thinner SEI compared to BE counterpart. Additionally, the small difference in the atomic concentration values after 100 cycles suggests a minor increase

26884062, 2024, 4, Downloaded from https://onlinelibrary.wiley.com/doi/10.1002/sstr.202300425 by Forschungs/

centrum Jülich GmbH Research Center, Wiley Online Library on [07/05/2024]. See the Terms

conditions) on Wiley Online Library for rules of use; OA articles are governed by the applicable Creative Commons License



134

[DFTFSI]

Binding energy (eV)

400

Binding energy (eV)

BE+DFTFSI

BE+DFTFSI

Intensity (CPS)

Intensity (CPS)

N 1s

S 2p

132

396

Figure 6. Selected fitted XPS spectra of the harvested graphite (left) and NMC811 (right) electrodes using the BE + DFTFSI electrolyte after the formation cycles (blue) and after 100 cycles (black).

Binding energy (eV)

134

Binding energy (eV)

BE+DFTFSI

402

BE+DFTFSI

170

400

Binding energy (eV)

166

Binding energy (eV)

ntensity (CPS)

Intensity (CPS)

132

396

26884062, 2024, 4, Downloaded from https://onlinelibrary.wiley.com/doi/10.1002/sstr.202300425 by Forso

Research Center, Wiley Online Library on [07/05/2024]. See the Terms

in SEI thickness during galvanostatic cycling. Furthermore, the peaks assigned to organic species from C 1s core spectra are less pronounced or even not observable during etching. From the F 1s, N 1s, and S 1s core spectra of the graphite electrode with BE + DFTFSI, the inorganic solid species of LiF, Li₂S, and Li₃N are the main constituents in the inner part of the SEI (Figure S10, S12, and S13, Supporting Information). [23] Overall, organic decomposition products are the main

components in the outer layer of the SEI, while the inorganic species are the main components in the inner layer. In the case of the BE, a large amount of LiF can be observed in the inner layer, while Li₂S, and Li₃N are dominant in the inner layer for BE + DFTFSI. Li₃N has a high ionic conductivity and together with mechanically stable LiF, a highly conductive SEI layer with good mechanical properties can be expected to form in the case of cells containing a BE + DFTFSI electrolyte that results

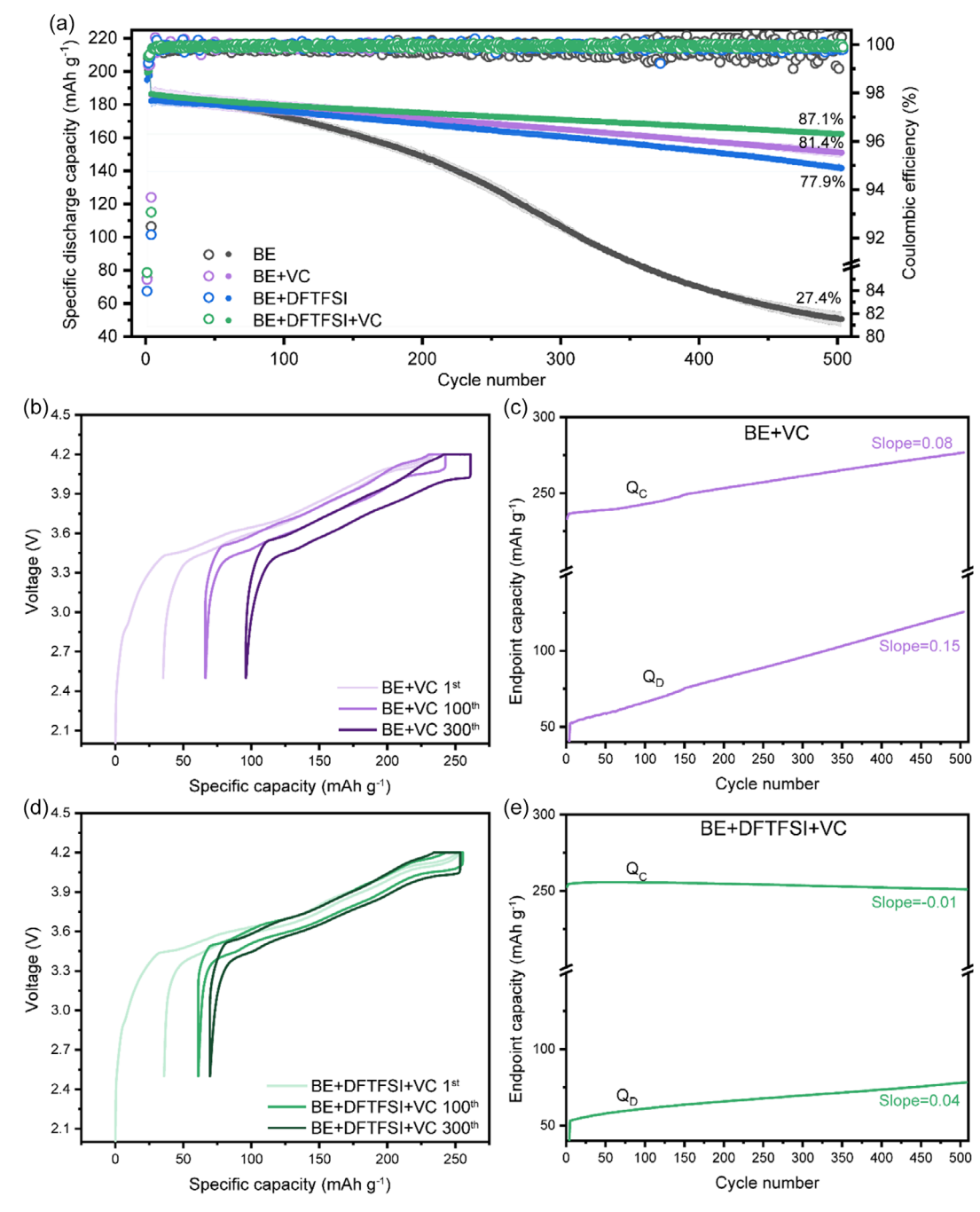


Figure 7. a) Specific discharge capacities and Coulombic efficiencies of NMC811||graphite cells with considered electrolytes as a function of cycle number, 80% SOC is considered as the end of life. Electrochemical charge-discharge profile of NMC811||graphite cells in b) BE + VC and d) BE + DFTFSI + VC. The charge and discharge endpoints of considered cells with c) BE + VC and e) BE + DFTFSI + VC are plotted using cumulative capacity versus cycler number.

on Wiley Online Library for rules of use; OA articles are governed by the applicable Creative Commons

small structures

www.advancedsciencenews.com www.small-structures.com

in the improved performance observed during galvanostatic cycling. [24,51,52]

In conclusion, the positive contribution of LiDFTFSI to both SEI and CEI can be proven. However, it is not sufficient to stabilize the corresponding interphases for long-term galvanostatic cycling, as an increased deterioration rate is observed after $\approx\!250$ cycles. The cross-talk from the anode to the cathode and the continuous electrolyte consumption lead to the growth of inhomogeneous CEI and LLI, thus resulting in the knee point for the cell containing BE + DFTFSI.

2.2. Synergistic Effect Between LiDFTFSI and VC

To further advance the electrochemical performance of NMC811||graphite cell chemistry, the well-known film-forming additive, vinylene carbonate (VC), was introduced to the BE+DFTFSI electrolyte in a concentration of 2 wt% (BE+DFTFSI+VC). For a fair comparison, the corresponding formulation without LiDFTFSI (BE+VC) was considered as reference.

Figure 7a clearly demonstrates that with the addition of VC, the NMC811||graphite cells containing BE + VC achieve 81.4%

capacity retention after 500 cycles with a specific discharge capacity of 151.3 mAh g^{-1} . This notable improvement can be attributed to the SEI film-forming ability of VC on the graphite surface. [14,15,53] Remarkably, the addition of VC in BE + DFTFSI leads to the highest capacity retention of 87.1% among the considered counterparts after 500 cycles, reaching SOH_{80%} after 720 cycles (Figure S3, Supporting Information). This observation highlights the synergistic effect of LiDFTFSI and VC, indicating their ability to notably enhance the electrochemical performance of the considered cells. Upon analyzing the charge-discharge profile of selected cycles in Figure 7b,d, it is noticeable that the cell containing BE + DFTFSI + VC only exhibits a slight increase in overvoltage during galvanostatic cycling compared to cells using all other electrolyte formulations considered. Moreover, when evaluating the capacity endpoints Q_C and Q_D of cells containing the considered electrolyte, the previously observed distinct knee point at approximately 250 cycles for the cell containing BE + DFTFSI (Figure 1e) is found to disappear in the presence of VC (Figure 7e). Post mortem studies on electrodes containing BE + DFTFSI in the previous section concluded that the knee point arises from the growth of an inhomogeneous CEI. The disappearance of the knee point for the cell containing BE + DFTFSI + VC can be attributed to the formation of more

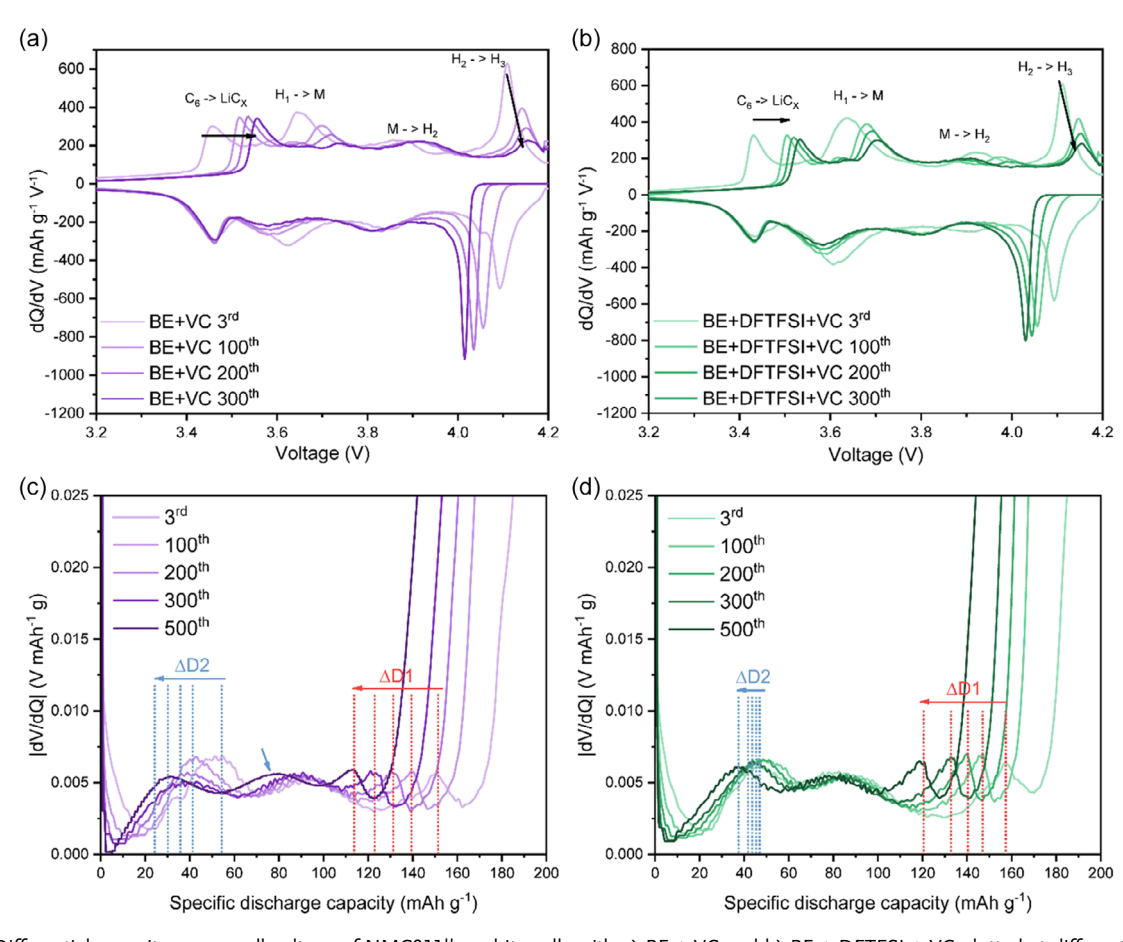


Figure 8. Differential capacity versus cell voltage of NMC811||graphite cells with a) BE + VC and b) BE + DFTFSI + VC plotted at different cycles. The peaks are assigned to their corresponding phase transition. [65] M represents the monoclinic phase and H_1 , H_2 , and H_3 represent the hexagonal phases. $C_6 \rightarrow LiC_x$ arises from the lithiation of graphite active material. Differential voltage versus discharge capacity of NMC811||graphite cells with c) BE + VC and d) BE + DFTFSI + VC at different cycles.

small structures

www.advancedsciencenews.com www.small-structures.com

effective interphases and therefore, reduced electrolyte decomposition, which is enabled by the synergy between LiDFTFSI and VC. Furthermore, the lowest slope of endpoint Q_D compared to other considered cells suggests the suppression of side reactions at the anode, supporting the formation of an effective SEI. Moreover, in comparison to the cell containing BE shown in Figure 1c, the cell containing BE + VC exhibits a stable marching of both Q_C and Q_D with a lower slope. This behavior indicates a classic aging phenomenon characterized by continuous SEI growth.^[27] The observed trend aligns with the positive effect of VC on the graphite surface and SEI formation.

The ICA plots shown in **Figure 8**a,b, reveal a small peak shift and slow decrease in peak intensity assigned to the $C_6 \rightarrow LiC_X$ transition during galvanostatic cycling for cells containing either BE+VC or BE+DFTFSI+VC, which indicates the good structural stability of the graphite electrode enabled by both electrolytes. However, a notable difference arises in the peak assigned to the $H_1 \rightarrow M$ phase transition. For the LIB cell containing BE+VC, the intensity of this peak almost disappears after 300 cycles, suggesting that the NMC811 electrode exhibits similar structural behavior to the previous cases. In contrast, the cell containing BE+DFTFSI+VC exhibits an intensity

retention of this peak, indicating the superior structural stability of the cathode enabled by the presence of BE + DFTFSI + VC. A similar trend can be observed in the DVA plots shown in Figure 8c,d, as a comparatively large $\Delta D2$ for the cell with BE + VC, but an almost constant $\Delta D2$ is evident for the cell with BE + DFTFSI + VC. It is worth noting that for the cell with BE + VC, the large $\Delta D2$ can already be observed from the 3rd to the100th cycle, whereas for the cell with BE + DFTFSI (Figure 3e), $\Delta D2$ shows minor changes during the initial cycles and starts increasing after 200 cycles. While the effect of VC alone may not be as pronounced as that of LiDFTFSI in the initial stages of galvanostatic cycling, it still shows the positive effect on the cathode compared to BE, as confirmed by the ICA and DVA analysis.

The systematic post-mortem analysis enables the separate study of the synergistic effect between LiDFTFSI and VC on the graphite and NMC811 electrodes. By comparing the impedance values shown in **Figure 4** and **9**, it becomes apparent that in the case of BE + VC containing cell, the VC acts on the graphite electrode, resulting in a more resistive SEI compared to BE (7.3 Ω vs 4.7 Ω). Additionally, a difference in the appearance of deposits can also be observed on the graphite particle surface

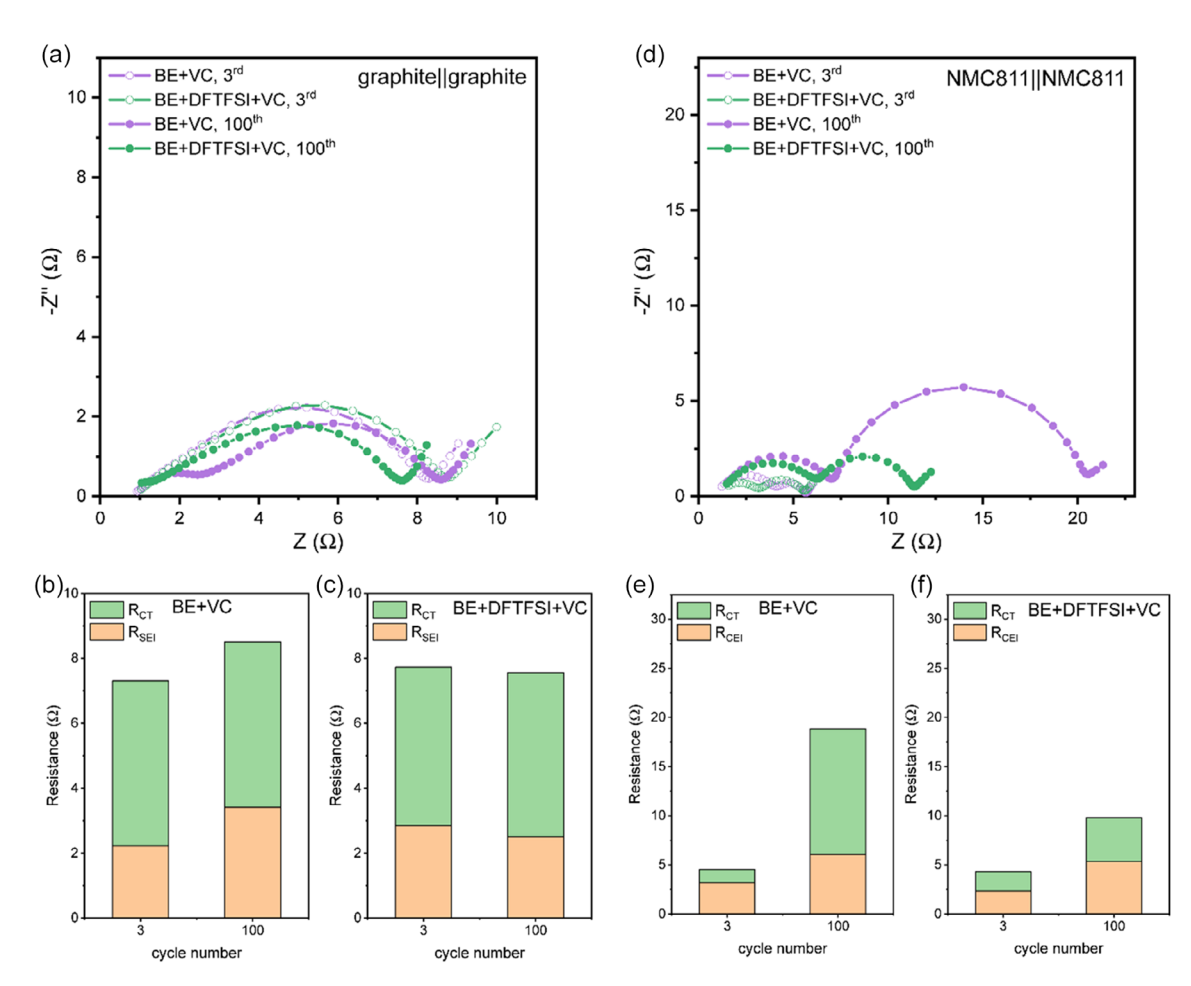


Figure 9. a) Nyquist plots for reassembled symmetric graphite cells after three formation cycles and after 100 cycles and fitted resistance for b) BE + VC and c) BE + DFTFSI + VC. d) Nyquist plot for reassembled NMC811||NMC811 cells after three formation cycles and after 100 cycles and fitted resistance for e) BE + VC and f) BE + DFTFSI + VC.

from https://onlinelibrary.wiley.com/doi/10.1002/sstr.202300425 by Forschungsa

centrum Jülich GmbH Research Center, Wiley Online Library on [07/05/2024]. See the Term

www.advancedsciencenews.com

www.small-structures.com

by SEM (Figure S5a,b, Supporting Information). Through the further addition of LiDFTFSI to the electrolyte, similar impedance values were observed for BE + DFTFSI + VC compared to BE + VC counterpart (7.7 vs 7.3 Ω) on the graphite electrode. As discussed in the previous section, the cell containing BE + DFTFSI showed an increased R_{CEI} resistance and decreased R_{CT} compared to BE, suggesting the presence of a resistive CEI with a lower energy barrier for charge transfer. Interestingly, upon the addition of 2 wt% VC to the electrolyte, an evident decrease of R_{CEI} (BE + DFTFSI: 5.1 Ω ; BE + DFTFSI + VC: 2.4 Ω) along with an increase of R_{CT} (BE + DFTFSI: 0.8Ω ; BE + DFTFSI + VC: 2Ω) was observed on the NMC811 electrode after the formation cycles (Figure 9d). Moreover, unlike in previous cases, the resistance growth is only minor after 100 cycles, indicating the formation of an effective and less resistive CEI originating from the synergistic effect between LiDFTFSI and VC. In addition, SEM images show that a smooth and homogenous surface layer formed on the NMC811 electrode with BE + DFTFSI + VC after the formation cycles, which remains unchanged after 100 cycles (Figure S5g,h, Supporting Information). This observation is in stark contrast to the inhomogeneous deposition observed on NMC811 electrode with BE + DFTFSI, as shown in Figure S4g,h, Supporting Information. In conclusion, the distinct knee point observed by the cell containing BE+DFTFSI is effectively suppressed upon the addition of VC. The suppression of the knee point can be attributed to the superior structural stability of NMC811 electrode, as evidenced by the ICA and DVA studies. The enhanced structural stability of NMC811 electrode is enabled by the homogenous, effective, and robust CEI. The synergistic effect between LiDFTFSI and VC plays a crucial role in achieving this enhanced stability and performance of the resulting NMC811||graphite cell chemistry.

To gain further insights into the decomposition product of VC and the synergistic effect between VC and LiDFTFSI, XPS analysis was conducted on harvested graphite and NMC811 electrodes from cells containing BE + VC and BE + DFTFSI + VC electrolytes after the formation cycles. As shown in **Figure 10**, compared to VC-free electrolytes in Figure 5, the majority of decomposition products from the electrolyte solvent and

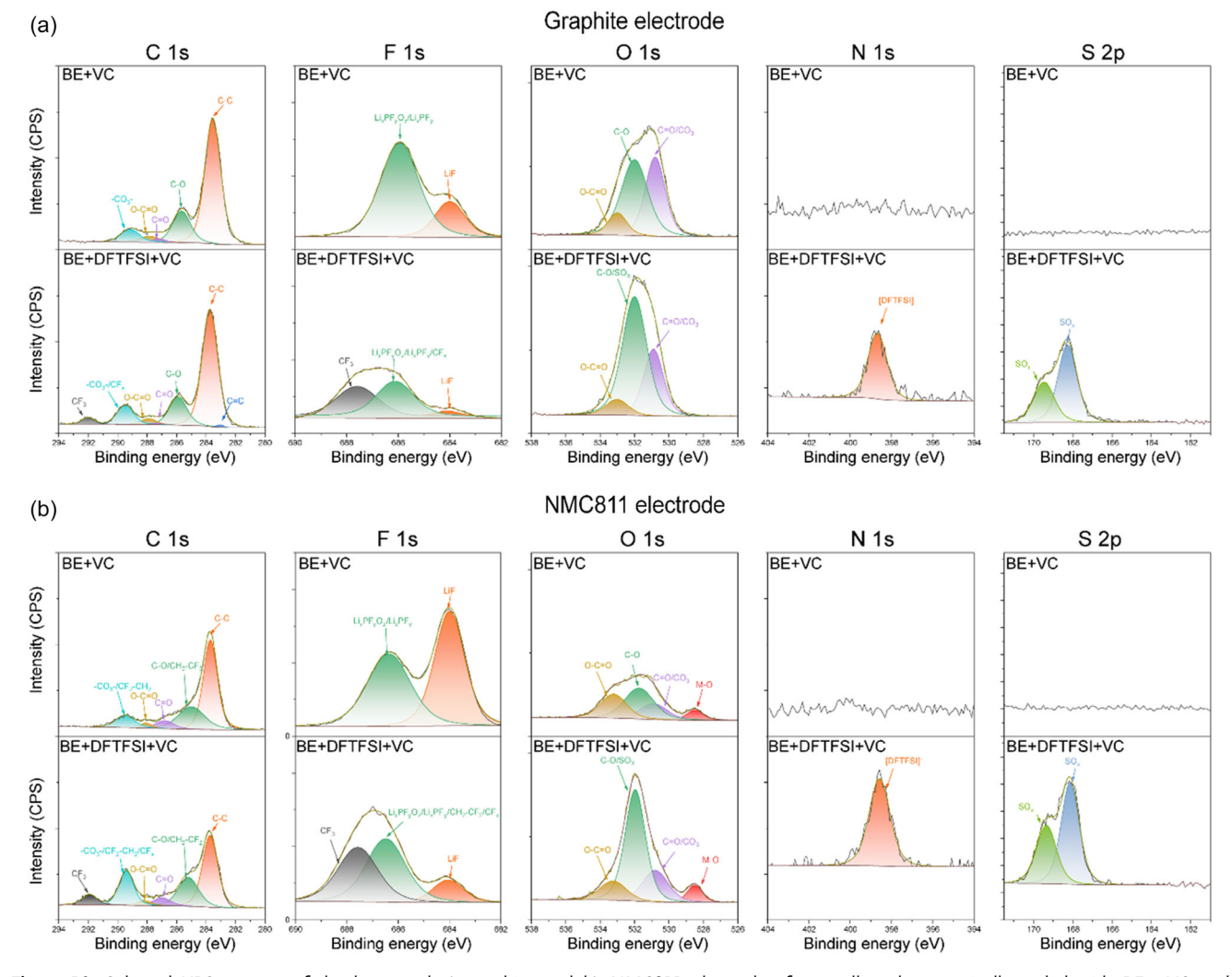


Figure 10. Selected XPS spectra of the harvested a) graphite and b) NMC811 electrodes from cells galvanostatically cycled with BE + VC and BE + DFTFSI + VC after the formation cycles.

26884062, 2024, 4, Downloaded from https://onlinelibrary.wiley.com/doi/10.1002/sstr.202300425 by Forsch

Research Center, Wiley Online Library on [07/05/2024]. See the Terms

conducting salts are identical due to the similar structure of EC and VC molecules. [54,55] However, VC is known for its polymerization to poly(VC) with repeating EC units on the anode surface. [55] Analyzing the C 1s spectra from the XPS measurement, a higher relative intensity of the peak assigned to –CO₃–is observed for graphite electrodes in the case of BE + VC compared to BE, indicating the formation of poly(VC) on the graphite

surface. In addition, a higher intensity of the peak assigned to

C–O from C 1s and O 1s core spectra is observed for graphite electrode with BE + VC, indicating the decomposition of VC. [55] Furthermore, it is interesting to note that the intensity of the $-\text{CO}_3-$ peak remains unchanged whereas the intensity of the C–O peak increases for the NMC811 electrode in the case of BE + VC compared to BE counterpart. Based on this observation, it can be deduced that the polymerization of VC predominantly takes place on the graphite surface, whereas the decomposition

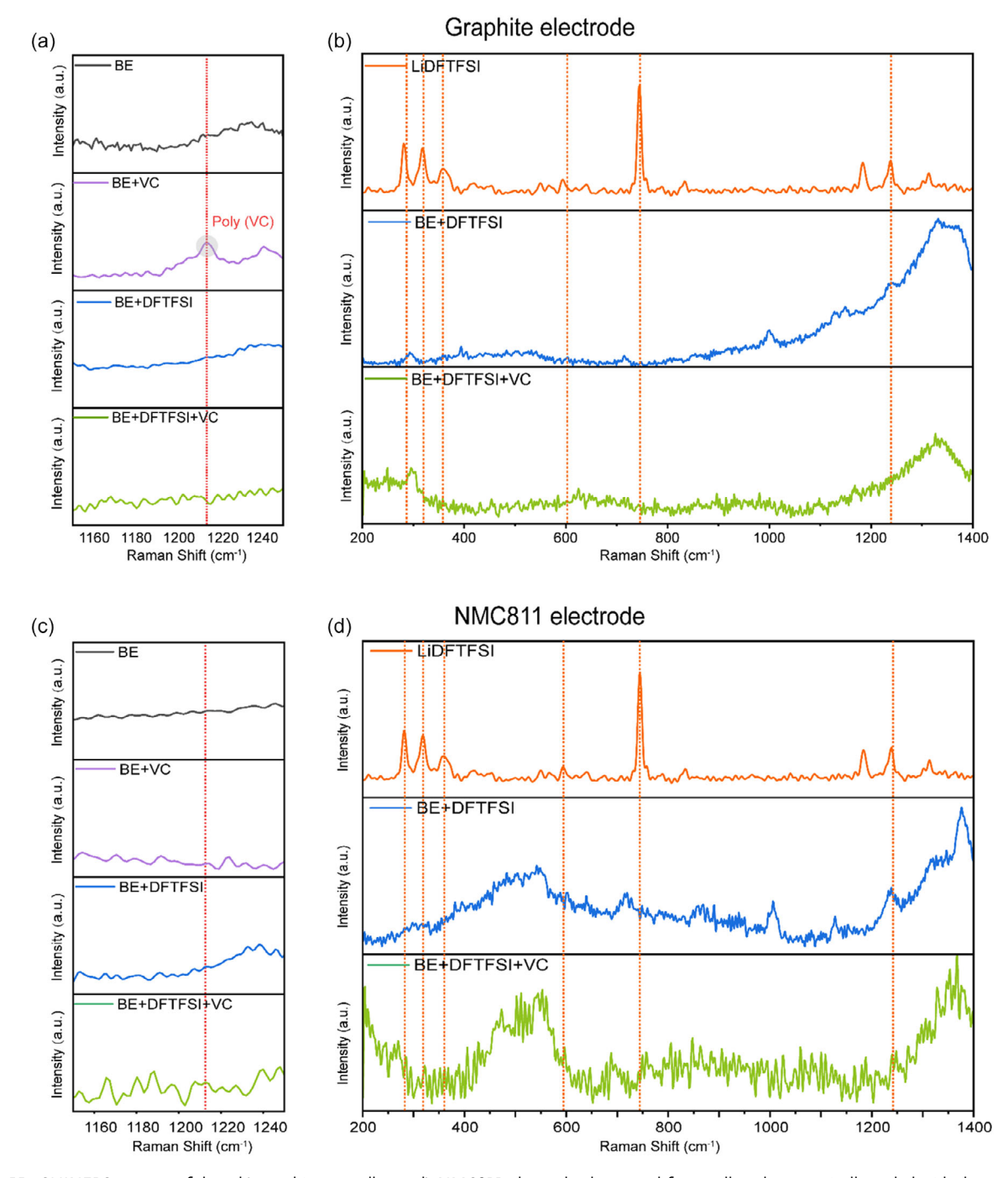


Figure 11. SHINERS spectra of the a,b) graphite as well as c,d) NMC811 electrodes harvested from cells galvanostatically cycled with the considered electrolytes after the formation cycles.

26884062, 2024, 4, Downloaded from https://onlinelibrary.wiley.com/doi/10.1002/sstr.202300425 by Forschungs/

entrum Jülich GmbH Research Center, Wiley Online Library on [07/05/2024]. See the Terms

conditions) on Wiley Online Library for rules of use; OA articles are governed by the applicable Creative Commons License

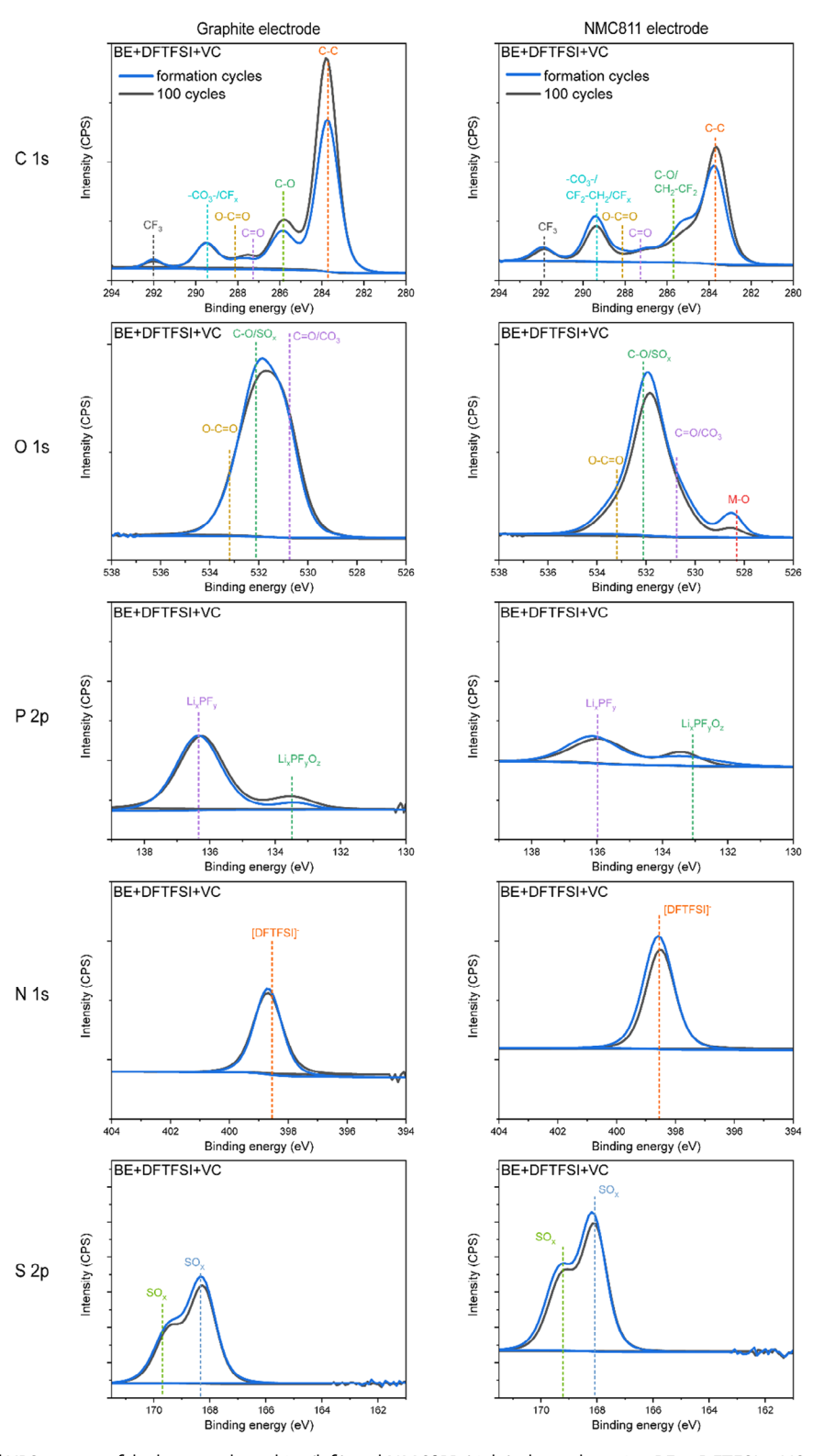


Figure 12. Selected fitted XPS spectra of the harvested graphite (left) and NMC811 (right) electrodes using BE + DFTFSI + VC electrolyte after formation cycles (blue) and after 100 cycles (black).

www.advancedsciencenews.com www.small-structures.com

products of VC can also be detected on the NMC811 electrode surface.

Additional post-mortem SHINERS investigations were conducted on the interphases of the graphite and NMC811 electrodes after formation cycles to gain a comprehensive understanding of the composition of the SEI and CEI formed in the presence of LiDFTFSI and VC. The full-range spectra of the graphite and NMC811 electrodes with details of peak assignment are listed in the supplementary information (Figure S16 and S17, Supporting Information). Figure 11a shows the magnification of the spectra of graphite electrodes. Notably, a band observed around 1142 cm⁻¹ can be attributed to poly(VC) for graphite electrodes in the case of BE + VC, while it was absent in the case of BE + DFTFSI + VC. Additionally, bands assigned to different LiDFTFSI decomposition products were observed around 277, 332, 360, 602, 747, and 1240 cm⁻¹ for the graphite electrode in the case of BE + DFTFSI (Figure 11b). Upon the further addition of VC, the bands assigned to the decomposition products from LiDFTFSI are found to be less distinct compared to BE + DFTFSI counterpart. Moreover, the band attributed to poly(VC) was not observed on the NMC811 electrode in the case of BE + VC (Figure 11c), indicating that the polymerization of VC only takes place on the graphite surface. In addition, bands assigned to the decomposition products from LiDFTFSI were less distinct for the NMC811 electrode in the case of BE + DFTFSI + VC (Figure 11d). These observations support a synergistic effect between LiDFTFSI and VC, impacting both the graphite and NMC811 electrodes.

To further confirm the positive effect of the synergistic effect between LiDFTFSI and VC on graphite and the NMC811 electrode performance, XPS measurements were conducted for both graphite and NMC811 electrodes harvested from cells galvanostatically cycled with BE + DFTFSI + VC after 100 cycles to study the surface composition changes. Figure 12 shows the results for graphite electrodes. A slightly increased peak assigned to C-O from C 1s core spectra after 100 cycles suggests the further decomposition of VC during galvanostatic cycling. Depth profiling revealed that the graphite electrodes containing VC-added electrolytes has no signal of C=C before etching and displayed a substantially low atomic concentration after etching (Figure S15, Supporting Information). This suggests a relatively thick SEI surface for graphite electrodes from cells with VC-added electrolytes compared to BE and BE + DFTFSI electrolytes. Moreover, a further decrease in atomic concentration after 100 cycles indicates SEI growth. For the graphite electrode harvested from cells containing BE + DFTFSI + VC shown in Figure 12, the peak assigned to the CF₃ from C 1s core spectra retains a constant intensity during galvanostatic cycling. In addition, there are no changes evident for the peaks assigned to the SO_x from S 2p core spectra and [DFTFSI]⁻ from N 1s core spectra, after 100 cycles. This is in contrast to the case of BE + DFTFSI, indicating the effective SEI contributed by VC. For NMC811 electrodes, the peaks that are assigned to the LiDFTFSI or its decomposition products either remain constant or slightly decrease after 100 cycles. In combination with the relatively unchanged peaks related to the solvents and LiPF₆ salt, it can be concluded that an effective CEI is formed on the NMC811 electrode. Comparing the thicknesses of the CEI, in the case of BE + DFTFSI + VC the electrodes exhibit only minor

increases in CEI thickness after 100 cycles (1.2-2 nm) in contrast to BE + VC (2.7-4 nm) and BE + DFTFSI (1.6-3.5 nm). This indicates the formation of a thin and effective CEI enabled by the synergy of LiDFTFSI and VC. It also suggests that the cross-talk effect, which leads to an inhomogeneous thick CEI, is mitigated by the synergistic effect between LiDFTFSI and VC. These findings are also in agreement with the results obtained from EIS and SEM analysis, which show that BE + DFTFSI + VC leads to an effective, homogenous, and less resistive surface layer on NMC811 electrodes.

3. Conclusions

In summary, we showed that an enhanced galvanostatic cycling performance of NMC811||graphite cells can be achieved by utilizing LiDFTFSI and LiPF6 in a blended salt organic carbonatebased electrolyte formulation. The results obtained demonstrate that LiDFTFSI facilitates the formation of modified interphases on both graphite and NMC811 electrodes, contributing to the improved structural stability of both electrodes and reduced cell polarization over 250 charge/discharge cycles. However, the growth of an inhomogeneous CEI, caused by the well-known cross-talk between both LIB electrodes, adversely affected long-term cycling stability. To address this, VC was introduced to the LiDFTFSI + LiPF₆ containing electrolyte, thus resulting in the advanced galvanostatic cycling performance of the resulting cell chemistry. Complementary ICA, DVA and EIS analysis indicated superior structural stability and minimal resistance of the NMC811 cathode during cell performance. Additionally, systematic post-mortem SEM, XPS and Raman analysis of the graphite and NMC811 electrodes revealed the positive synergistic effect of LiDFTFSI and VC on both electrodes. This synergy eliminates the cross-talk effect and promotes the formation of effective and uniform SEI and CEI. Our findings provide valuable insights into the complex interplay between electrolyte components and their valuable impact on the overall cell chemistry and its performance, offering a potential path forward for the further development of advanced electrolytes for Li-based batteries.

4. Experimental Section

Electrolyte Components and Resulting Formulations: Potassium trifluoromethylsulfonimide and difluoromethanesulfonyl chloride were synthesized in accordance with known procedures. [56,57] For LIDFTFSI, a modified synthetic route was chosen compared to the literature.^[58] Ethylene carbonate (EC), ethyl methyl carbonate (EMC), VC, and LiPF₆ were purchased in battery-grade quality from E-Lyte Innovations GmbH and were used as received. 1 M LiPF₆ in EC:EMC (3:7 by weight) was used as a BE. Two different stock solutions were formulated by mixing EC and EMC in a ratio of 3:7 with/without 2% VC. All electrolytes considered were formulated by adding lithium salt to the selected stock solution in a volumetric flask. The resulting formulations are listed in Table 1.

Synthesis of LiDFTFSI: Potassium trifluoromethylsulfonimide (78.1 g, 417 mmol) and imidazole (56.8 g, 834 mmol) were dissolved in dry acetonitrile (400 mL). Difluoromethanesulfonyl chloride (HCF₂SO₂Cl) (62.8 g, 417 mmol, 1.0 eq.) was added to the solution and the resulting slurry was heated to 70 °C overnight. The next portion of HCF₂SO₂Cl (12.5 g, 0.2 eq.) was added and the mixture was stirred at reflux for 3 h. The third portion of HCF₂SO₂Cl (6.2 g, 0.1 eq.) was added, with the reaction mixture being

www.small-structures.com

Table 1. Considered electrolyte formulations.

Abbreviation	Electrolyte formulations
BE	1 м LiPF ₆ in EC:EMC (3:7 by weight)
BE + DFTFSI	$0.5\mathrm{M}$ LiPF $_{6}+0.5\mathrm{M}$ LiDFTFSI in EC:EMC (3:7 by weight)
BE + VC	1 м LiPF $_{\rm 6}$ in EC:EMC (3:7 by weight) $+2\%$ VC
BE + DFTFSI + VC	$0.5\mathrm{M}$ LiPF $_6+0.5\mathrm{M}$ LiDFTFSI in EC:EMC
	(3:7 by weight) $+2\%$ VC

stirred at reflux for 3.5 h, thereafter at room temperature overnight. The reaction mixture was filtered, the precipitate was washed with acetonitrile $(3 \times 50 \text{ mL})$, and the washings were combined with the mother liquor and concentrated under a reduced pressure to yielded approx. 190 g of a brown oil. The oil was dissolved in water (400 mL) and treated with concentrated HCl (75 mL). The aqueous layer was then extracted with diethyl ether $(4 \times 120 \text{ mL})$. The combined extracts were dried over Na₂SO₄ and concentrated under a reduced pressure. The crude product was treated with a solution of KOH (19.9 g, 0.85 eq.) in water (200 mL) until pH 5-6. The solution was washed with diethyl ether (2 × 20 mL) and the ethereal washings were discarded. The aqueous phase was evaporated under reduced pressure to dryness. The obtained semi-solid material (KDFTFSI) was triturated with diethyl ether, which left the crude potassium salt as a lightbrown crystalline solid (59.4 g). The crude salt was dissolved in water (80 mL) and the solution was treated with concentrated HCl (70 mL). The resulting solution was extracted with diethyl ether (4 \times 80 mL) and the organic extracts were washed with brine (2 × 30 mL) and dried over Na₂SO₄. After the removal of the solvent under a reduced pressure, a brown liquid (70 g) was obtained. Pure (difluoromethanesulfonyl) (trifluoromethanesulfonyl)imide (HDFTFSI) was obtained by sublimation of the crude material in a vacuum as a colorless, highly hygroscopic, crystalline solid (37.9 g, 34%).

HDFTFSI (37.9 g, 140.7 mmol) was dissolved in water (100 mL). A solution of LiOH·H₂O (5.87 g, 140.0 mmol) in water (50 mL) was added, and the resulting solution was concentrated under a reduced pressure. The resulting syrup was absorbed in toluene (400 mL), and the mixture was heated to reflux with a Dean-Stark head overnight. Toluene was decanted, and the remaining highly viscous residue was dried for 4 h at 80 °C in a vacuum. The resulting white cake was quickly crushed in a mortar, and the obtained powder was dried for 7 h at 120 °C in a high vacuum. The product was transferred to a dry box, where it was again crushed in a mortar. The fine powder obtained was dried for 8 h at 130 °C in a high vacuum to leave LiDFTFSI as a colorless, amorphous powder (36.2 g, 96%). The nuclear magnetic resonance (NMR) spectral data are in full accordance with previously published data. [58]

¹H NMR (400 MHz, DMSO – d6):
$$\delta = 6.62 (t, J = 53.4 \text{ Hz}) \text{ ppm}$$
 (3)

13
C NMR (101 MHz, DMSO $-$ d6):

$$\delta = 119.8 (q, J = 322.0 \text{ Hz}), 113.6 (t, J = 277.3 \text{ Hz}) \text{ ppm}$$
 (4)

$$\delta = -78.3 \text{ (s, 3F)}, -124.0 \text{ (d, } J = 53.4 \text{ Hz) ppm}$$
(5)

Electrodes and Cell Assembly: Calandered NMC811 single-sided coated cathode sheets with an areal capacity of 1.0 mAh cm $^{-2}$ were provided by Umicore. Calandered graphite single-sided coated electrode sheets with an areal capacity of 1.14 mAh cm $^{-2}$ were provided by CIDETEC, corresponding to an N/P ratio of 1.14. The electrodes were cut into ø14 mm and ø15 mm disks for the cathode and the anode, respectively. The electrodes were subsequently dried at 120 °C under vacuum ($<10^{-2}$ mbar) for 12 h and stored in the argon-filled glovebox before cell assembly. Li metal (500 µm thickness) purchased from China Energy Lithium CO. Ltd was kept inside the argon-filled glovebox as well. Coin

cell parts (stainless steel 316) were purchased from Xiamen TOB New Energy Technology Co. Ltd. As separator, Celgard 2500 for 2032-type coin cell assembly and Whatman grade GF/D for Swagelok-type cells assembly, before being dried overnight at 60 °C and stored in the argon-filled glovebox.

CR2032 coin-type two electrode cells were assembled by placing Celgard 2500 as a separator between the graphite anode and the NMC811 cathode with a fixed, previously calculated amount of electrolyte (30 μ L). $^{[59]}$ The complete cell stack consisted of the following: wave spring (1.4 mm), spacer (1 mm), anode, first electrolyte portion (15 μ L), separator, second electrolyte portion (15 μ L), cathode, spacer (0.5 mm). Swagelok-type cells were used for the three-electrode setup and were assembled using Ø12 mm NMC811 as a working electrode, Ø12 mm graphite as a counter electrode and Ø13 mm Whatman grade GF/D as separator. Li metal was used as a reference electrode and separated by Ø10 mm Whatman grade GF/D. In total, a 200 μ L electrolyte was soaked in the separator. All cells were assembled in an argon-filled glovebox.

Electrochemical Characterization: The constant current-constant voltage (CC-CV) charge and constant current discharge cycling performance of NMC811||graphite full cells^[60] were evaluated on a battery tester (MACCOR series 4000) in a voltage range from 2.5 to 4.2 V at 20 °C. C-rates were calculated individually for each cell from the cathode mass and the theoretical capacity. The cell formation conditions comprised of 3 cycles at 0.1 C. The cells were then galvanostatically cycled for 500 cycles at 1 C to evaluate the galvanostatic cycling performance. For each electrolyte, at least three cells were assembled and evaluated to ensure reproducibility, as indicated by error bars in the respective figures throughout the manuscript.

Electrochemical Impedance Spectroscopy: Electrochemical impedance spectroscopy (EIS) measurements were carried out at a Bio-Logic VMP3 workstation in a frequency range of 10 mHz–1 MHz after 30 min of rest time. The coin cells were galvanostatically cycled and charged to 50% state-of-charge (SOC). The full cell impedance was measured and the coin cells were subsequently disassembled. Symmetric cells with 30 μL of the same electrolyte were reassembled and impedance spectra of the symmetric cells were recorded. $^{[40]}$

Raman Spectroscopy: To gain a deeper insight into the interphases on electrochemically aged electrodes, Raman spectroscopy was performed using a confocal Raman microscope (Horiba Scientific, LabRAM HR evolution, air-cooled CCD detector) with a 600 line mm⁻¹ grating. The samples were excited with red (633 nm, 10.5 mW) and green (532 nm, 19 mW) lasers, adjusted by a 10% filter to limit the laser power to 1.05 mW and 1.9 mW, respectively. A 50X long-working distance objective (Carl Zeiss Microscopy, 9.22 mm, numerical aperture 0.5) was used to focus the beam, and spectra were collected for 25 s with four accumulations. The Raman microscope was operated using LabSpec 6.6.2.7 software (Horiba Scientific) for data collection and treatment. Prior to the measurements, the system was calibrated on the peak of crystalline silicon at a Raman shift of 520.7 cm⁻¹. Peak assignment was performed based on the peaks identified in the raw spectra, as shown in the Supplementary Information.

Shell-Isolated Nanoparticle-Enhanced Raman Spectroscopy (SHINERS) Sample Preparation: The ${\rm SiO_2}$ -coated nanoparticles with a size of 55 nm used for SHINERS were synthesized and characterized according to the studies of Pfeiffer et al. [61–63] After synthesis and purification, the nanoparticles were drop-casted on the glass windows of the air-tight optical cells (EL-CELL, ECC-Opto-Std). The windows were dried to remove moisture and transferred to an argon-filled glovebox for cell assembly. During assembly of the optical cell, the electrode samples were brought into contact with the nanoparticles on the glass window to obtain the near-field enhancement of the SHINERS technique for interphase analysis. The electrodes under consideration were collected from NMC811||graphite coin cells that were galvanostatically cycled for three formation cycles at a rate of 0.1 C between 2.5 and 4.2 V without any washing.

Scanning Electron Microscopy: Both anode and cathode were analyzed via scanning electron microscopy (SEM) after three formation cycles and after 100 cycles. The cells under consideration were opened in an argon-filled glovebox and the electrodes were rinsed with EMC (1 mL)

ADVANCED SCIENCE NEWS

www.advancedsciencenews.com

www.small-structures.com

to remove the residual electrolyte. Electrodes were then transferred to the SEM chamber using a vacuum-sealed sample holder and analyzed using an Auriga CrossBeam workstation (*Zeiss*) at an acceleration voltage of 3 kV and a working distance of 3 mm using the InLens detector.

X-Ray Photoelectron Spectroscopy: To prevent exposure to oxygen and moisture, the X-ray photoelectron spectroscopy (XPS) samples were sealed in vials after preparation. The sealed vials were opened in a glovebox connected to the instrument shortly before the measurement. XPS measurements were performed on an Axis Ultra DLD spectrometer (Kratos Analytical, UK) equipped with a monochromatic Al K_{α} source $(E_{photon} = 1486.6 \text{ eV})$ at a 0° angle of emission using a 10 mA emission current and an accelerating voltage of 12 kV for the X-ray source. The hemispherical analyzer was set to a pass energy of 20 eV. The analyzed area was approximately 700 µm × 300 µm ("hybrid" lens mode, "slot" aperture), and a charge neutralizer was utilized to compensate for sample charging. During measurements, the pressure within the analysis chamber was always lower than 1×10^{-7} mbar. Sputter depth profiling of the negative electrodes was conducted using monoatomic argon at an energy of 500 eV. The depth profiling procedure consisted of two sputter cycles of 360 s each. Two samples of each type (pristine samples, samples that had been in contact with the electrolyte, formatted samples and cycled samples) were measured to ensure reproducibility. For peak fitting, the CasaXPS software (Casa Software, UK) was used[64] and the peaks were assigned based on known literature values. [22-24] The energy scale in the spectra was adjusted using the F 1s peak at 684.0 eV (LiF) as an internal reference.

Supporting Information

Supporting Information is available from the Wiley Online Library or from the author.

Acknowledgements

The authors acknowledge funding from the European Union's Horizon 2020 research and innovation program under Grant Agreement Nos. 957189 (BIG-MAP) and 957213 (BATTERY2030PLUS).

Conflict of Interest

The authors declare no conflict of interest.

Data Availability Statement

The data that support the findings of this study are available from the corresponding author upon reasonable request.

Keywords

blended salt electrolyte, electrode|electrolyte interface, Ni-rich layered cathode, synergistic effect

Received: October 16, 2023 Revised: November 28, 2023 Published online: December 26, 2023

- [1] R. Schmuch, R. Wagner, G. Hörpel, T. Placke, M. Winter, *Nat. Energy* **2018**, *3*, 267.
- [2] W. Xue, M. Huang, Y. Li, Y. G. Zhu, R. Gao, X. Xiao, W. Zhang, S. Li, G. Xu, Y. Yu, P. Li, J. Lopez, D. Yu, Y. Dong, W. Fan, Z. Shi, R. Xiong,

- C.-J. Sun, I. Hwang, W.-K. Lee, Y. Shao-Horn, J. A. Johnson, J. Li, *Nat. Energy* **2021**, *6*, 495.
- [3] K. Guo, S. Qi, H. Wang, J. Huang, M. Wu, Y. Yang, X. Li, Y. Ren, J. Ma, Small Sci. 2022, 2, 2100107.
- [4] K. Xu, Chem. Rev. 2004, 104, 4303.
- [5] H. Chen, J. Liu, X. Zhou, H. Ji, S. Liu, M. Wang, T. Qian, C. Yan, Chem. Eng. J. 2021, 404, 126470.
- [6] S. Nowak, M. Winter, J. Electrochem. Soc. 2015, 162, A2500.
- [7] A. Blyr, A. Du Pasquier, G. Amatucci, J.-M. Tarascon, *Ionics* 1997, 3,
- [8] D. R. Gallus, R. Schmitz, R. Wagner, B. Hoffmann, S. Nowak, I. Cekic-Laskovic, R. W. Schmitz, M. Winter, Electrochim. Acta 2014, 134, 393.
- [9] Q. Liu, Z. Chen, Y. Liu, Y. Hong, W. Wang, J. Wang, B. Zhao, Y. Xu, J. Wang, X. Fan, L. Li, H. B. Wu, Energy Storage Mater. 2021, 37, 521.
- [10] S. Tan, Z. Shadike, J. Li, X. Wang, Y. Yang, R. Lin, A. Cresce, J. Hu, A. Hunt, I. Waluyo, L. Ma, F. Monaco, P. Cloetens, J. Xiao, Y. Liu, X.-Q. Yang, K. Xu, E. Hu, Nat. Energy 2022, 7, 484.
- [11] D. R. Gallus, R. Wagner, S. Wiemers-Meyer, M. Winter, I. Cekic-Laskovic, *Electrochim. Acta* 2015, 184, 410.
- [12] J.-N. Zhang, Q. Li, Y. Wang, J. Zheng, X. Yu, H. Li, Energy Storage Mater. 2018, 14, 1.
- [13] S. Fang, D. Jackson, M. L. Dreibelbis, T. F. Kuech, R. J. Hamers, J. Power Sources 2018, 373, 184.
- [14] M. Nie, J. Demeaux, B. T. Young, D. R. Heskett, Y. Chen, A. Bose, J. C. Woicik, B. L. Lucht, J. Electrochem. Soc. 2015, 162, A7008.
- [15] L. Martin, H. Martinez, M. Ulldemolins, B. Pecquenard, F. Le Cras, Solid State Ionics 2012, 215, 36.
- [16] S. Hong, B. Hong, W. Song, Z. Qin, B. Duan, Y. Lai, F. Jiang, I. Electrochem. Soc. 2018, 165, A368.
- [17] L. A. Dominey, V. R. Koch, T. J. Blakley, *Electrochim. Acta* 1992, 37, 1551.
- [18] X. Fan, X. Ji, L. Chen, J. Chen, T. Deng, F. Han, J. Yue, N. Piao, R. Wang, X. Zhou, X. Xiao, L. Chen, C. Wang, Nat. Energy 2019, 4, 882.
- [19] K. Xu, Chem. Rev. 2014, 114, 11503.
- [20] L. Li, S. Zhou, H. Han, H. Li, J. Nie, M. Armand, Z. Zhou, X. Huang, J. Electrochem. Soc. 2011, 158, A74.
- [21] M. Morita, T. Shibata, N. Yoshimoto, M. Ishikawa, J. Power Sources 2003, 119-121, 784.
- [22] L. Qiao, U. Oteo, M. Martinez-Ibañez, A. Santiago, R. Cid, E. Sanchez-Diez, E. Lobato, L. Meabe, M. Armand, H. Zhang, *Nat. Mater.* 2022, 21, 455.
- [23] A. Santiago, J. Castillo, I. Garbayo, A. Saenz de Buruaga, J. A. Coca Clemente, L. Qiao, R. Cid Barreno, M. Martinez-Ibañez, M. Armand, H. Zhang, C. Li, ACS Appl. Energy Mater. 2021, 4, 4459.
- [24] H. Zhang, U. Oteo, X. Judez, G. G. Eshetu, M. Martinez-Ibañez, J. Carrasco, C. Li, M. Armand, Joule 2019, 3, 1689.
- [25] J. Liu, T. Qian, N. Xu, M. Wang, J. Zhou, X. Shen, C. Yan, Energy Storage Mater. 2020, 24, 265.
- [26] X. Liu, T. Qian, J. Liu, M. Wang, H. Chen, C. Yan, Energy Storage Mater. 2019, 17, 260.
- [27] V. Meunier, M. Leal De Souza, M. Morcrette, A. Grimaud, Joule 2023, 7, 42.
- [28] R. D. Deshpande, P. Ridgway, Y. Fu, W. Zhang, J. Cai, V. Battaglia, J. Electrochem. Soc. 2015, 162, A330.
- [29] J. Xu, R. D. Deshpande, J. Pan, Y.-T. Cheng, V. S. Battaglia, J. Electrochem. Soc. 2015, 162, A2026.
- [30] H. M. Dahn, A. J. Smith, J. C. Burns, D. A. Stevens, J. R. Dahn, J. Electrochem. Soc. 2012, 159, A1405.
- [31] I. Bloom, A. N. Jansen, D. P. Abraham, J. Knuth, S. A. Jones, V. S. Battaglia, G. L. Henriksen, J. Power Sources 2005, 139, 295.
- [32] H. Kato, Y. Kobayashi, H. Miyashiro, J. Power Sources 2018, 398, 49.
- [33] J. Li, L. E. Downie, L. Ma, W. Qiu, J. R. Dahn, J. Electrochem. Soc. 2015, 162. A1401.

www.small-structures.com

- [34] W. M. Dose, J. K. Morzy, A. Mahadevegowda, C. Ducati, C. P. Grey, M. F. L. De Volder, J. Mater. Chem. A 2021, 9, 23582.
- [35] J. Zhu, W. Xu, M. Knapp, M. S. Dewi Darma, L. Mereacre, P. Su, W. Hua, X. Liu-Théato, H. Dai, X. Wei, H. Ehrenberg, Cell Rep. Phys. Sci. 2023, 4, 101464.
- [36] J. Wang, J. Purewal, P. Liu, J. Hicks-Garner, S. Soukazian, E. Sherman, A. Sorenson, L. Vu, H. Tataria, M. W. Verbrugge, J. Power Sources **2014**, *269*, 937.
- [37] J. Zhu, M. S. Dewi Darma, M. Knapp, D. R. Sørensen, M. Heere, O. Fang, X. Wang, H. Dai, L. Mereacre, A. Senyshyn, X. Wei, H. Ehrenberg, J. Power Sources 2020, 448, 227575.
- [38] E. Björklund, C. Xu, W. M. Dose, C. G. Sole, P. K. Thakur, T.-L. Lee, M. F. L. De Volder, C. P. Grey, R. S. Weatherup, Chem. Mater. 2022, 34, 2034.
- [39] O. C. Harris, S. E. Lee, C. Lees, M. Tang, J. Phys.: Energy 2020, 2, 032002.
- [40] R. Petibon, C. P. Aiken, N. N. Sinha, J. C. Burns, H. Ye, C. M. VanElzen, G. Jain, S. Trussler, J. R. Dahn, J. Electrochem. Soc. 2013, 160, A117.
- [41] S. Solchenbach, X. Huang, D. Pritzl, J. Landesfeind, H. A. Gasteiger, J. Electrochem. Soc. 2021, 168, 110503.
- [42] M. Gaberscek, J. Moskon, B. Erjavec, R. Dominko, J. Jamnik, Electrochem. Solid-State Lett. 2008, 11, A170.
- [43] D. Pritzl, A. E. Bumberger, M. Wetjen, J. Landesfeind, S. Solchenbach, H. A. Gasteiger, J. Electrochem. Soc. 2019, 166, A582.
- [44] I. Landa-Medrano, A. Eguia-Barrio, S. Sananes-Israel, S. Lijó-Pando, I. Boyano, F. Alcaide, I. Urdampilleta, I. De Meatza, J. Electrochem. Soc. 2020, 167, 090528.
- [45] D. W. Abarbanel, K. J. Nelson, J. R. Dahn, J. Electrochem. Soc. 2016, 163, A522.
- [46] N. R. Vadivel, S. Ha, M. He, D. Dees, S. Trask, B. Polzin, K. G. Gallagher, J. Electrochem. Soc. 2017, 164, A508.
- [47] A. Tornheim, R. Sahore, M. He, J. R. Croy, Z. Zhang, J. Electrochem. Soc. 2018, 165, A3360.
- [48] Y. S. Jung, P. Lu, A. S. Cavanagh, C. Ban, G.-H. Kim, S.-H. Lee, S. M. George, S. J. Harris, A. C. Dillon, Adv. Energy Mater. 2013, 3, 213.

- [49] P. Niehoff, M. Winter, Langmuir 2013, 29, 15813.
- [50] S. Malmgren, K. Ciosek, R. Lindblad, S. Plogmaker, J. Kühn, H. Rensmo, K. Edström, M. Hahlin, Electrochim. Acta 2013, 105, 83,
- [51] A. Santiago, X. Judez, J. Castillo, I. Garbayo, A. Sáenz De Buruaga, L. Qiao, G. Baraldi, J. A. Coca-Clemente, M. Armand, C. Li, H. Zhang, J. Phys. Chem. Lett. 2020, 11, 6133.
- [52] M. Ikeya, J. Phys. Soc. Jpn. 1977, 42, 168.
- [53] D. Pritzl, S. Solchenbach, M. Wetjen, H. A. Gasteiger, J. Electrochem. Soc. 2017. 164. A2625.
- [54] B. L. D. Rinkel, D. S. Hall, I. Temprano, C. P. Grey, J. Am. Chem. Soc. **2020**, 142, 15058.
- [55] A. L. Michan, B. S. Parimalam, M. Leskes, R. N. Kerber, T. Yoon, C. P. Grey, B. L. Lucht, Chem. Mater. 2016, 28, 8149.
- [56] A. S. L. Gouveia, E. Malcaitè, E. I. Lozinskaya, A. S. Shaplov, L. C. Tomé, I. M. Marrucho, ACS Sustainable Chem. Eng. 2020, 8, 7087
- [57] X.-J. Tang, C. S. Thomoson, W. R. Dolbier, Org. Lett. 2014, 16, 4594.
- [58] U. Oteo, M. Martinez-Ibañez, I. Aldalur, E. Sanchez-Diez, J. Carrasco, M. Armand, H. Zhang, ChemElectroChem 2019, 6, 1019.
- [59] B. R. Long, S. G. Rinaldo, K. G. Gallagher, D. W. Dees, S. E. Trask, B. J. Polzin, A. N. Jansen, D. P. Abraham, I. Bloom, J. Bareño, J. R. Croy, J. Electrochem. Soc. 2016, 163, A2999.
- [60] R. Nölle, K. Beltrop, F. Holtstiege, J. Kasnatscheew, T. Placke, M. Winter, Mater. Today 2020, 32, 131.
- [61] F. Pfeiffer, D. Diddens, M. Weiling, M. Baghernejad, ACS Appl. Mater. Interfaces 2023, 15, 6676.
- [62] F. Pfeiffer, D. Diddens, M. Weiling, L. Frankenstein, S. Kühn, I. Cekic-Laskovic, M. Baghernejad, Adv. Mater. 2023, 13, 2300827.
- [63] B. A. Sadeghi, C. Wölke, F. Pfeiffer, M. Baghernejad, M. Winter, I. Cekic-Laskovic, J. Power Sources 2023, 557, 232570.
- [64] N. Fairley, V. Fernandez, M. Richard-Plouet, C. Guillot-Deudon, J. Walton, E. Smith, D. Flahaut, M. Greiner, M. Biesinger, S. Tougaard, D. Morgan, J. Baltrusaitis, Appl. Surf. Sci. Adv. 2021, 5. 100112.
- [65] R. Jung, M. Metzger, F. Maglia, C. Stinner, H. A. Gasteiger, J. Electrochem. Soc. 2017, 164, A1361.